THESIS

SCALE-DEPENDENT WEAR AND RE-ROUGHENING PROCESSES IN A SINGLE FAULT ZONE

Submitted by

Katherine Shervais

Department of Geoscience

In partial fulfillment of the requirements

For the Degree of Master of Science

Colorado State University

Fort Collins, Colorado

Summer 2015

Master's Committee:

Advisor: James D. Kirkpatrick

Peter Nelson
Derek Schutt

ABSTRACT

SCALE-DEPENDENT WEAR AND RE-ROUGHENING PROCESSES IN A SINGLE FAULT ZONE

One factor that exerts a major control on earthquake source parameters is the geometry of a fault zone. Observations previously compiled from multiple faults show that fault surface shape evolves with displacement. The specific processes driving fault evolution within a single fault zone and their influence on fault geometry are not well known. Here, we characterize the deformation history and geometry of an extraordinarily well-exposed fault using maps constructed with the Structure from Motion photogrammetric method. The geometry of cross sectional traces of contacts of different relative age was analyzed with power spectral density and variogram calculation. The last slip zone to form in the fault is smoothest of any surface and is distinct from other surfaces, recording significant smoothing on a single structure and localization of strain onto thinner layers. We infer that smoothing occurred abruptly due to localization of slip onto a new slip zone rather than as a result of progressive wear of a fault surface. Continuous wear from processes such as grain plucking and sliced asperities also smoothed surfaces at scales larger than the clast dimension, and also re-roughened surfaces at scales smaller than the clast dimension. Additionally, periodic variations in fault thickness define the characteristic asperity size and are a signature of wear on the fault surface. Scale dependent smoothing and re-roughening and the interplay between these processes explain the varying geometry of immature and mature faults. The evolution of roughness and asperity size we observe can explain differences in the source characteristics of earthquakes as faults mature.

ACKNOWLEDGEMENTS

This project was completed due to support from many people. I would especially like to thank my advisor, Dr. Jamie Kirkpatrick, for his thoughtful and patient discussion and input. In addition, I would like to thank Dr. Peter Nelson and Dr. Derek Schutt for their time and consideration as members of my committee, my field assistants Anna Hissem and Dr. John Shervais, Boyd Deep Canyon Nature Reserve and Dr. Al Muth, Dan Brogan for RTK-DGPS technical support, Dr. Michael Ronayne for frequent discussion and guidance, and the CSU Department of Geoscience for supporting my graduate studies as well as the Southern California Earthquake Center for supporting my field research.

TABLE OF CONTENTS

Chapter 1: Introduction

Earthquake nucleation and slip is controlled by the geometry of fault surfaces. Faults lock on geometric asperities, build up stress, fail, slip seismically, resulting in stress release, and then lock again (Reid, 1910; Scholz, 1998). Asperities are bumps on the fault surface; the size of the asperities defines the areas of contact of the opposing sides of a fault. Asperity contacts define the maximum friction of the fault surface, as they are the sites of high normal stress and are most likely to fail in shear. As the ratio of shear to normal stress on the fault surface approaches and surpasses the coefficient of static friction of the asperities in contact, asperities fail elastically or inelastically leading to fault slip (Scholz, 1998). The type of failure is dependent on the aspect ratio and length of the asperity in relation to the strength of the asperity material. The strength of asperities has a direct impact on the static fault strength as well as the dynamic shear resistance on a fault (Chester and Chester, 2000; Brodsky and Kanamori, 2001; Di Toro *et al.*, 2006). Constraining the scale(s), characteristics and spatial variability of asperities could lead to a greater understanding of both static strength and dynamic shear resistance of seismic faults.

Asperity scale can be quantified in terms of a fault's roughness, or the height of a given point on a fault surface or trace in reference to the mean fault plane (Archard, 1953). Studies of fault surface roughness that map the topography of slickensides with tools such as ground-based LiDAR indicate there is a continuous scaling of roughness of fault surfaces (e.g. Sagy *et al.*, 2007). In cross-sections through a fault surface, as the length scale of observation increases, the size of the largest asperity on the fault surface also increases. However, fault surfaces are thought to be self-affine rather than self-similar, so they scale differently in the fault plane and normal to the fault plane.

When a fault first propagates as a newly formed fracture, it is typically well-matched, meaning the two sides of the fault interlock perfectly (Brodsky and Kanamori, 2001; Davidesko *et al.*, 2014). Asperities on either side of the fault will essentially be entirely in contact. After asperity failure and fault slip occurs, asperities again "lock" the fault, but fault surfaces are mismatched. The mismatch is equal to the amount of slip. At this point, the fault surface roughness is likely similar on either side of the fault.

When a fault is mismatched, the space between the two sides of the fault is typically not empty – it is filled with wear material generated by the slip of the fault, called fault rock, or veins. Wear processes on the fault surface produce fault rock during slip, a result of the interaction between the two opposing sides of the fault (Power *et al*., 1988). Fault rock can be ultra/cataclasite (cohesive wear material), pseudotachylyte (frictional melt from wear) or gouge (non-cohesive wear material) (Sibson, 1977). The shape of the fault rock between the two layers reflects the shape of the fault surface on either side at that point. The classically held hypothesis in structural geology suggests that fault thickness, determined by the roughness of the fault at a large wavelength scale, scales linearly on a log-log plot with increasing displacement (Childs *et al.*, 2009). Because fault core thickness is dependent on the roughness of the fault surface (as the fault material fills in the gaps between the hanging wall and footwall), the gouge should be thicker when the fault surface has larger asperities. However, field observations of large-slip faults rarely show fault cores of a thickness greater than ten meters, which implies at some wavelength scale the mechanical behavior of the fault changes and fault rock is no longer produced or little is produced relative to the scale of the fault itself.

Fault length increases over multiple slip events but also maintains a roughly constant ratio with displacement (Cowie and Scholz, 1992). Therefore, large-slip faults are expected to exhibit a lengthy slip history and accumulate fault rock from multiple events. Studying the evolution of fault characteristics over multiple slip events is difficult as it is relatively hard to constrain products of discrete slip events because of their extremely similar characteristics, though some have investigated the smoothing of fault surfaces with increasing displacement (Sagy *et al.*, 2007; Sagy and Brodsky, 2009; Brodsky *et al.*, 2011).

The Boyd Fault, in the Santa Rosa Mountains south of Palm Desert, CA, presents a unique opportunity to examine the history of an ancient seismic fault and its evolution. This fault exhibits stratified layers of fault gouge of varying thicknesses with crosscutting relationships and discontinuous layers. These characteristics allow the relative timing, and therefore evolution with displacement, of the structures to be inferred. Individual layers could have formed during a single slip event, but may have been re-used by many. Older layers have been deformed by later slip events, but the contacts of the fault core are continuous as are the contacts of a single layer within the fault core. To characterize the evolution of the fault with displacement, we study both the most recent slip event as well as the fault core as a whole to constrain characteristics of the fault that evolve with slip, the processes that wear on the fault surface, and the characteristic asperity size of the fault surface.

Chapter 2 of this thesis has been prepared in the format of a journal article with the intention that it will be submitted for publication. In section 2.1, I introduce the study by detailing past work and the outstanding questions that motivated this study. Section 2.2 establishes a tectonic context for the Boyd Fault. Section 2.3 details my field methods and results. Section 2.4 details the geometric analysis methods and results, including power spectaral

density and variogram calculations. Section 2.5 presents an interpretation of the deformation history and discussion of the results in the context of this fault zone and previous studies. Chapter 3 outlines potential future work linked to this study.

Chapter 2: Scale-dependent wear and re-roughening processes in a single fault zone

2.1. Introduction

The non-planar shape, or roughness, of fault surfaces exerts a fundamental control on fault strength and stability (Byerlee, 1978; Lay *et al.*, 1982; Aki, 1984; Power *et al.*, 1988; Scholz, 2002). Contact and mechanical interaction of asperities across a fault impact earthquake nucleation, slip distribution, dynamic weakening processes, near- fault stress fields and source parameters such as moment release, radiated energy and stress drop (Chester and Chester, 2000; Brodsky and Kanamori, 2001; Parsons, 2008; Griffith *et al.*, 2010; Dunham *et al.*, 2011; Shi and Day, 2013). Measurements of exposed surfaces using profiling tools show that the asperities, or bumps, that define fault roughness range in size from micrometers to hundreds of meters and that roughness is self-affine (scales differently in the fault plane and normal to the fault plane) over a wide range of scales of observation (*e.g.* Renard *et al.*, 2006; Sagy *et al.*, 2007; Candela *et al.*, 2012).

Roughness measurements also show that fault surfaces of mature faults are smoother than immature faults, and all surfaces are smoother in the slip-parallel direction compared to the slip perpendicular direction (Candela *et al.*, 2012). These observations imply that fault surface geometry evolves with displacement towards smoother profiles, but compilations of roughness measurements from many faults suggest the smoothing occurs at a gradual rate, perhaps due to inefficient wear processes (Power *et al.*, 1987; Sagy *et al*., 2007; Brodsky *et al*., 2011). One key missing constraint is the evolution of roughness over the deformation history of a single fault zone, which has never been measured (Brodsky *et al.*, 2011).

Wear processes on the fault surface cause the evolution of geometry of the surface and have been interpreted previously as transient, or reflecting a high rate of wear, in natural systems due to the fractal nature of fault surfaces (Power *et al.*, 1988). The interaction between asperities and failure of asperities at all scales on opposing sides of a fault controls fault friction and strength, but the failure of asperities also results in an evolving fault surface. If wear processes are continuous, the smoothing of a fault surface should be proportional to displacement. However, as varying fault geometry is linked to varying normal stress, the evolution of asperities on the surface results in spatially heterogeneous and evolving normal stress (Dieterich and Linker, 1992; Linker and Dieterich, 1992). Experimental work has shown that wear rates are dependent on normal stress as well as shear stress (Wang and Scholz, 1994; Boneh *et al.*, 2013; Lyakhovsky *et al.*, 2014). In addition, wear processes on fault surfaces have been shown to be scale-dependent in experimental work (Boneh *et al.*, 2014; Davidesko *et al.*, 2014). Varying wear rate due to normal stress and the scale of observation may result in complex wear processes on fault surfaces, resulting in fault geometry that does not become as smooth as expected (Sagy and Brodsky, 2009; Brodsky *et al.*, 2011; Boneh *et al.*, 2013). Elastic and inelastic deformation of the fault surface also results in scale-dependent wear processes, as asperities break at one scale but may glide past each other at another scale (Wang and Scholz, 1994; Kirkpatrick and Brodsky, 2014). However, scale-dependent wear processes have rarely been observed in the field (Sibson, 1986; Scholz, 1987; Wang and Scholz, 1994; Wilson *et al.*, 2003). Understanding wear processes on fault surfaces is significant, as these processes change the geometry of the fault surface as it slips by breaking or grinding asperities at all scales, and therefore influence the mechanical behavior of a fault.

In this study, we take advantage of exceptional exposures of a fault that contains evidence for multiple generations of slip events. Because the fault is exposed in cross section rather than as a fault slickenside, we can use crosscutting relationships and mineral assemblages to interpret the deformation history of the fault and identify the oldest preserved slip surfaces and the most recent slip surface. We measure the roughness of the edges of the slip surfaces over length scales from centimeters to ten meters. We quantify and describe scale-dependent wear processes within the fault core that both smooth and re-roughen the fault surface, resulting in a "wear signature" of periodic fault traces. As the fault core geometry evolves, the asperities on the surface evolve as well. These insights are used to identify the characteristic asperity size for the most recent slip event(s) on a likely seismogenic fault.

2.2 Geologic Setting:

The Boyd Fault crops out in Coyote Canyon in the Eastern Peninsular Ranges of southern California, one of the bounding mountain ranges of the Coachella Valley (Fig. 2.1a) (Rowe *et al.*, 2012; previously described as the Coyote Creek fault by Wenk *et al.*, 2000 and the La Quinta Fault by Matti *et al.*, 2006). The fault has an average orientation of 297/17° NE based on 14 measurements of slickenside orientations along strike (Fig. 2.2b). Dip-slip slickenlines on exposed surfaces have an average rake of ~80° from the east. Continuous over a mapped trace length of 9.4 kilometers, the fault juxtaposes Asbestos Mountain tonalite in the hanging wall and Palm Canyon Metamorphic Complex in the footwall (Sharp, 1979). The Asbestos Mountain batholith varies in composition, but is generally described as a biotite-hornblende rich tonalite containing a weak regional foliation (Morton *et al.*, 2014). The Palm Canyon Metamorphic Complex is a deformed metasedimentary complex composed of a variety of gneisses (anatectic gneiss, orthogneiss, mylonitic gneiss) as well as migmatites, pelitic schists, amphibolites,

pyroxenties, and marbles (Morton *et al.*, 2014; Sharp, 1967). Our study focuses on fault exposures in Coyote Canyon and the area adjacent to the mouth of Deep Canyon (Fig. 2.1b). The extent of the fault to the north of the study area, and beyond Martinez Mountain landslide to the south is unknown, but is thought to continue for ~30 km (Fig. 2.1a) (Matti *et al.*, 2006).

Regionally, the fault is parallel to the nearby Santa Rosa Mylonite Zone (SRMZ), but is structurally higher (Fig. 2.1a)(Goodwin and Renne, 1991). The hanging wall of the mylonite zone is composed of either Asbestos Mountain tonalite or Palm Canyon Complex. Thermal histories derived from fission track, $^{40}Ar/^{39}Ar$, K/Ar, and U/Pb ages for the Asbestos Mountain tonalite and the Palm Canyon Complex adjacent to the SRMZ suggest cooling was rapid and that both reached a temperature of <300° by 70 Ma, likely constraining the earliest time of activity for the Boyd fault (Armstrong and Suppe, 1973; Dokka, 1984; Goodwin and Renne, 1991; Wenk *et al.*, 2000). This is supported by $^{40}Ar/^{39}Ar$ dating of pseudotachylytes from the hanging wall and footwall of the Boyd Fault, which indicate brittle faulting during the Laramide at ~56-62 Ma as well as potential periods around ~70 Ma and 39 Ma (Wenk *et al.*, 2000). Orientations of the pseudotachylytes suggest they formed during reverse slip events (Fig. 2.2c)(Wenk *et al.*, 2000).

Field evidence indicates a post-Laramide phase of deformation on the Boyd Fault, but few direct timing constraints are available for this. Our observations show that the Laramide pseudotachylytes are consistently offset by normal-sense shear fractures and subsidiary faults, but when they formed is unknown (Fig. 2.2c). Multiple parallel faults dipping shallowly towards the east-northeast of a similar scale or greater than the Boyd Fault, including the West Salton Detachment Fault ~25 km to the south, exist in the region that have been interpreted as Laramide-era thrusts reactivated as extensional detachment structures in the Miocene (Axen and Fletcher, 1998; Rowe *et al.*, 2012). However, basal conglomerates on fault dip-slopes and

piercing points that were used to delimit Miocene extension are not present for the Boyd Fault in Coyote Canyon (Dorsey *et al.*, 2011; Janecke *et al.*, 2010), possibly because of rapid uplift in the Santa Rosa Mountains or erosion along the fault trace. In addition to this potentially complex deformation history, we have not found any piercing points to measure the net displacement. Based on scaling relationships, a trace length of 10 km suggests a displacement of the order of a hundred meters, and if the fault is around 30+ km, the displacement would be more (*e.g.* Cowie and Scholz, 1992).

2.3. Field Observations of the Boyd Fault

The Boyd Fault is extraordinarily well exposed due to erosion at the base of Coyote Canyon (Fig. 2.2a). The fault has a distinctive internal architecture consisting of an ultracataclasite-filled inner fault core, an outer fault that is crosscut by the inner fault core, and an extensive damage zone (Rowe *et al.*, 2012). In total, the fault core has an approximate thickness of 12-15 meters, varying along strike due to fluctuations of both inner and outer fault core thickness. The entire fault width is ~75 m due to the extent of the damage zone. The outer fault core contains cataclasites that are crosscut by subsidiary faults. Multiple layers of crosscutting, discontinuous ultracataclasite define the inner fault core. All of the ultracataclasite layers truncate other layers, indicating that each was a slip zone at some stage during the deformation history. One continuous ultracataclasite layer within the inner fault core, referred to here as layer d, crosscuts all other deformation structures, and is interpreted as the slip zone for the most recent event on the fault.

2.3.1 Field and microstructural methods

Five extensive exposures of the Boyd Fault were selected for this study that provided a high percentage of exposed fault (56.5%) relative to covered areas (43.5%) over a 167 m span. These exposures are located at the base of cliffs in the riverbed of Coyote Canyon, which trends ~305°, approximately the strike direction of the fault. The exposure lengths are 34.9 m, 4.58 m, 27.7 m, 5.31 m and 21.9 m, and the trend of each is 17° or less off the strike direction.

We mapped the internal structure of the fault using high-resolution rectified images produced with the Structure from Motion (SfM) methodology. SfM uses traditional stereophotogrammetry techniques to build a 3D model with integrated color information of objects or scenes from photographs with large variations in location and view direction (Johnson *et al.*, 2014). After removing large debris and dirt covering the inner fault core, exposures were brushed with a fine brush to remove dust, small pebbles, and organic material. The exposures were then extensively photographed, with an average of 5 photographs per meter, and input into Agisoft's Photoscan Pro software (Fig. 2.3a,b). The program generated a 3D model with overlain texture (color) maps of each exposure by matching pairs of points in the images (see Supplementary Material for example model) (Verhoeven, 2011; Johnson *et al.*, 2014). High resolution (1.2 mm/pixel) orthorectified images of each exposure were created by rotating the models to view the exposures in the direction down the slip vector defined by slickenlines on exposed edges of the inner fault core and internal layers. The true thickness and geometry of the layers is apparent in the resulting cross sections through the fault.

The internal structure of the fault was mapped on an iPad in the field at each exposure. These maps were used to measure the geometry and interpret the deformation history of the

Boyd Fault (Fig. 2.3c) (Appendix A). The traces of contacts between the inner-outer fault core, as well as all identifiable layers within the inner fault core were mapped. The contacts between the inner and outer fault core were defined by texture, grain size and composition differences (see below). Layers within the inner fault core were mapped based on their grain size, color, cohesion, fracture characteristics, clast composition, and frequency of clasts (similar to Chester and Chester, 1998). Real-time kinematic (RTK) differential GPS ground control points (accurate to 1-2 mm) at the ends of each exposure were used to scale the traces to true exposure length, providing a physical meaning to subsequent observations of fault core geometry.

Measurements of the fault, outer fault core and damage zone structure orientations and kinematics were recorded within 1-2 m of the fault and at locations 11 m, 60 m, and 120 m above the fault in the hanging wall. In addition, the orientations of subsidiary faults in the footwall were measured. Lenticular clasts within the inner fault core were individually photographed and their aspect ratios, composition, and location recorded. Samples of the extremely friable ultracataclasites were collected by applying low viscosity resin to the exposures and carefully separating intact hand sample sized blocks. Thirty-five thin sections were prepared from these samples of slip zones and layers within the inner fault core to characterize microstructural deformation.

2.3.2 Fault zone architecture

The upper outer fault core is approximately 2 m thick and is composed of Asbestos Mountain tonalite that contains a foliation, cataclasites, dikes, shear fractures, and remnant pseudotachylyte veins. The foliation is defined by aligned biotites and hornblendes and is observed throughout the Asbestos Mountain batholith (Morton *et al.*, 2014). The foliation

orientation varies widely along strike and increases in intensity with proximity to the Boyd Fault. When oriented at an angle to the fault, it is truncated by ultracataclasite layers of the inner fault core. Dikes and pseudotachylytes both cut and exploit the foliation. Pseudotachylytes are present within the outer fault core near the fault (within 2 m) and in the damage zone (observed up to 60 m above the fault) with an average orientation of 192/39° W (Fig. 2.2c), indicating a wider range of orientations than was reported previously (Wenk *et al*., 2000). Cataclasites overprint the foliation and host rock so that the phaneritic texture is frequently no longer visible. At microscopic scale, the cataclasite is composed of shattered clasts of quartz and seriticized plagioclase with intact chlorite clasts (Fig. 2.6a). Cataclasite, foliation, dikes, and pseudotachylytes are crosscut by numerous high-angle normal-sense shear fractures. Shear fractures have a preferred orientation of 45/57° E-NE near to the fault (Fig. 2.2c).

The lower outer fault core is defined by the presence of cataclastically deformed Palm Canyon Complex cut by a system of minor faults. The region of minor faulting is approximately 10-15 m thick and is bound at its base by a subsidiary fault sub-parallel to the Boyd Fault in the main study area. Individual fault-bounded blocks in the lower outer fault core vary in texture, mineral composition, degree of deformation, degree of foliation, and color, but extensive quartz cementation means all are composed of cohesive fault rock. Microscopic texture of the lower outer fault core cataclasite is similar to the upper outer fault core cataclasite, with large (max. 4 mm) shattered clasts contained within an aphanitic matrix. Pseudotachylytes in the lower outer fault core appear at the edge of and within bands of cataclasite.

The inner fault core consists of 1-12 layers of ultracataclasite, each distinguishable from a combination of clast frequency, composition, and average size, as well as overall layer color and grain size (Fig. 2.2a). The inner fault core varies in total thickness from 8 to 75 cm (dependent

on the number of layers present) with an average thickness of 22 cm. Layer thickness varies from one millimeter (the thinnest layer) to over 40 centimeters (the thickest). Individual layers have spatially variable thickness, partially due to truncation of layers by later slip events. Layers are pale tan to dark brown, with shades of orange and red. Grain size of the matrix within the layers ranges from aphanitic, clay sized grains to sand sized grains. Frequency of clasts within the layers ranges from <10% clasts to 60% clasts in exposure. Clasts range from equidimensional to lenticular in shape and are composed of reworked inner fault core ultracataclasites, some from layers that are no longer present, as well as outer fault core cataclasite and tonalite. Some layers contain high-angle conjugate fractures spaced millimeters apart that terminate at layer edges; these cause the ultracataclasite to break into small (sub cm) blocks. Layers are interpreted as older when truncated by other layers, offset by shear fractures in the inner fault core, present as clasts within other layers, or some combination of the above. Generally, older layers have a larger grain size, larger clasts, and also tend to have less dense conjugate fracture networks or none at all, making these layers more cohesive. Relatively younger layers have a very fine grain size with smaller and less frequent clasts.

Lenticular clasts derived from the upper and lower outer fault cores and re-worked ultracataclasite layers are present in many of the layers of ultracataclasite (Fig. 2.4). Lenses were recognized as clasts with any aspect ratio significantly <1. They generally have a semi-elliptical shape, with one flat and one curved edge. They range in size from 4 cm to a maximum of 34 cm for tonalitic cataclasite and 3 cm to 90 cm for metasedimentary cataclasite. Lenses have a consistent aspect ratio across all lengths, which is dependent on material. Lenses of tonalitic cataclasite have a larger aspect ratio (0.32) (Fig. 2.4, right middle) than the metasedimentary cataclasite lenses (0.2) (Fig. 2.4, left middle). The orientation of the flat edge of the lenses also

varies. Both tonalitic and metasedimentary cataclasite lenses are observed with the flat edge of the clast facing towards their protolith and facing away from their protolith. The thickness of lenticular clasts is often similar to the thickness of the host ultracataclasite layers.

In general, the inner fault core crosscuts structures in the outer fault core. However, at Exposure 1 the outer fault core occasionally truncates layers of inner fault core ultracataclasite (Fig. 2.5a). At one location, only two ultracataclasite layers are continuous, including layer d, representing a thin region of the inner fault core. Additionally, the inner fault core is disrupted where conjugate subsidiary fractures in the upper outer fault core cut the contact between the inner and outer fault core. The thickness of the ultracataclasite is either significantly increased or decreased where this occurs depending on the subsidiary fracture orientation. This indicates the ultracataclasites deformed to fill the space created by syn-kinematic displacement on the subsidiary fractures (Fig. 2.5b, c).

In addition to the crosscutting relationships, petrographic and XRD analyses show that the inner and outer fault cores are mineralogically distinct (Appendix B). The upper (hanging wall) outer fault core is deformed tonalite that contains albite, quartz, anorthite, hornblende, biotite, chlorite group minerals (chlorite and chamosite), ± epidote, ± zeolite (laumontite), ± actinolite. The lower (footwall) outer fault core composition is more variable due to the variability in the Palm Canyon complex, but contains anorthite, quartz, albite, illite, epidote, ± chlorite group minerals (chlorite and chamosite), ± zeolite (laumontite) ± calcite. The inner fault core contains quartz, albite, labradorite, laumontite, chlorite, and chamosite. In addition, layer d (see below) contains a substantial amount of amorphous material and clay. The presence of chlorite, epidote, zeolite indicate alteration of amphiboles and biotite in both the upper and lower

outer fault cores. The inner fault core is distinct due to the absence of anorthite and presence of significant laumontite, indicating alteration at lower grade conditions than the outer fault core.

2.3.3 Layer d

Layer d is a distinct ultracataclasite layer that crosscuts all other layers of the inner fault core and, on occasion, the inner-outer fault core contacts (Fig. 2.6a, b and c). This layer is present at every exposure of the fault (unlike the other layers of ultracataclasite), and is always located adjacent to either the upper or lower edge of the inner fault core. It is the finest grained of any of the fault rocks, has a homogeneous composition, and varies in thickness from 0.1 to 8 cm. The edges of the layer are extremely planar at outcrop scale, except for rare cases where the layer splays around lenticular clasts of other fault rock, leading to a local increase in thickness and a local undulation of the surface (Fig. 2.6b). Ultracataclasite injection veins branch from layer d into the upper outer fault core (Fig. 2.6c). The injections typically have apertures comparable to the thickness of the layer, and ultracataclasite from the entire layer thickness is continuous with the ultracataclasite in the injections.

Layer d is composed of sub-rounded to rounded clasts (~0.05-0.1 mm diameter) in an aphanitic matrix. Thin section observations in cross polarized light show the matrix often displays a foliation defined by spaced phyllosilicate grains aligned parallel to the layer edges. In places, 1 to 4 mm thick bands where the entire matrix contains aligned phyllosilicates are present. However, the edges of these bands do not truncate clasts within the layer, and there is no other evidence for crosscutting relationships between the bands. Energy dispersive spectroscopy (EDS) maps show the proportion of elements is consistent across the layer (Fig. 2.7g). This

suggests the foliation and compositional banding are likely due to formation of a preferred phyllosilicate orientation within the layer during slip (*e.g.* Ujiie et al., 2013).

Clasts of quartz and feldspar with occasional clasts of chlorite and previously formed ultracataclasite make up a small percentage of the total composition of layer d (up to ~20%). Optically visible clasts have an average aspect ratio of 0.8 (n = 100). At high magnifications, clasts, as well as the grains composing the matrix, are angular to sub-angular, and show evidence of sub-micron scale fracturing (Fig. 2.7b, d, e). Clasts composed of the older layers of ultracataclasite and pseudotachylyte are occasionally present within layer d (Fig. 2.7b, f). The contact between layer d and the inner-outer fault core is generally planar at the grain scale, but includes local undulations where grains were plucked from the outer fault core (Fig. 2.7c).

2.4. Geometric Analysis

Power spectral density (Brown and Scholz, 1985; Power *et al*., 1988) and variogram analysis (see below) were used to quantitatively describe the geometry of the traces of the inner-outer fault core edges and upper and lower layer d contacts in the three largest exposures. The maximum length of calculation is one half the exposure length, so the two smaller exposures were too short to be included. Each trace was detrended to remove bias from the power spectral density and variograms. After detrending, data were resampled to constant point spacing. The vertical separation between the top and bottom of layer d as well as the top and bottom inner fault core contacts was calculated to create a thickness data set for layer d and the entire inner fault core within each exposure.

Because of the high percentage of exposure over the length of analysis, RTK-DGPS ground control points were also used to integrate the raw traces of each contact at all five

exposures into a single spatial reference frame, resulting in 167m-long traces for each contact. The combined traces were resampled to uniform point spacing, and covered portions between each exposure were filled with a linear interpolation based on the elevation change between exposure ends. The overall linear trend of the fault was removed from each combined trace, but not the trends local to individual exposures. The complete (167 m) data set for each trace with linear interpolation was used for power spectral density calculation. Interpolated segments comprise 43.5% of the combined traces, slightly above the 40% value that Candela *et al.* (2009) showed does not significantly impact the power spectral density calculation. The calculated power may be biased at long wavelengths, but the relationships between the traces are consistent with our results from individual exposures.

2.4.1 Power spectral density

The power spectral density (PSD) is a measure of the amplitudes of the spectral components of each contact trace. The trace geometries are consistent with a power law relationship between the PSD, $P(\lambda)$, and length scale, λ, of the form $P(\lambda)=C\lambda^{ß}$, where C is a constant and $ß$ is the average slope in log-log space. The power spectra were smoothed using the Welch method, which estimates the power spectra multiple times within overlapping windows of each trace and then averages the results (Welch, 1967).

The upper and lower outer fault core contacts have consistent power and slope within each of the three exposures analyzed, but the upper edge, adjacent to the hanging wall, is rougher (higher power) in all three exposures. Slopes vary slightly from exposure to exposure possibly due to small changes in the exposure trend compared to the fault strike (Table 2.1) (Fig. 2.8a, b, c). Variations from exposure to exposure are less significant than the relative roughness values

within each exposure. Our estimates of both *C* and *ß* are similar to values reported previously from LiDAR data (*e.g.* Sagy *et al.*, 2007; Bistacchi *et al.*, 2011; Candela *et al.*, 2012; Kirkpatrick and Brodsky, 2014), suggesting the results are robust.

The contacts bounding layer d have a different geometry than the inner-outer fault core edges (Fig. 2.8a, b, c). The PSD slopes for the d edges are similar to the inner-outer fault core edges. However, the upper and lower edges of layer d have the lowest power of any of the contacts over all wavelengths at each exposure showing that the layer d contacts are smoother than the inner-outer fault core contacts. The exception to this relationship is the lower outer fault core contact at exposure 1. Layer d is directly adjacent to the lower outer fault core contact over the entire extent of this exposure so the inner-outer fault core contact is the same as the edge of layer d (Fig. 2.8a).

Layer d is always located at the edge of the inner fault core so it forms contacts with both inner fault core ultracataclasites and outer fault core cataclasites. The type of contact correlates with the roughness of the trace at the edge of layer d. Where layer d is in contact with ultracataclasites, the edge of d is relatively smooth and where it is in contact with the cataclasites, the edge is rougher. This is apparent from the power spectra, which show that the layer d edges are asymmetric at Exposure 2 where layer d is located between the outer fault core and inner fault core (Fig. 2.8b). Layer d has the same roughness on either side at Exposure 1 because it occupies the entire width of the inner fault core for much of the exposure so is predominantly in contact with the outer fault core only. In addition, the roughness of the hanging wall edge of the inner fault core is the same at all three exposures, regardless of the location of d, while the roughness of the footwall edge of the inner fault core is smoother when adjacent to layer d at Exposure 1 (Fig. 2.8a).

Slopes of the PSD for the combined 167-m traces (avoiding spurious values at $\lambda > 11$ m) are slightly lower than the slopes for the individual exposures (Table 2.1) (Fig. 2.8d). The upper outer fault core PSD shows a break in slope at $\lambda = 0.9$ m. When the slope of this contact is calculated over the range $\lambda = 0.9$ - 11 m, it is 1.43, significantly lower than the slope of the PSD over the full data range. A significant break in slope is not observed for any of the other calculated traces when calculated over the same range (Table 2.1). This suggests the break in slope is not a result of artifacts within the data. The upper outer fault core contact has the highest power up to 2 m. As a result of the break in slope, the lower outer fault core contact has the highest power at greater wavelengths. These two traces have a higher power than the layer d traces.

2.4.2 Variogram analysis of natural and synthetic fault traces

The experimental semi-variogram (referred to here as the variogram) is a statistical function used to assess spatial continuity of data. The variogram, $\gamma(h)$ is one-half the experimental variogram, $2\gamma(h)$ calculated as:

$$\gamma(h) = \frac{1}{2N(h)} \sum_{i=1}^{N} [z(u+h) - z(u)]^2 \quad (1)$$

where $z(u)$ represents the value of some variable (such as layer thickness) at location $\underline{u}$, and $z(u+h)$ is the value of the same variable at location $u+h$, where h is the separation distance (m). This analysis is 1D (in the fault perpendicular direction), so u and h are scalar distances rather than vectors. The $N(h)$ in Equation (1) is the number of data pairs (e.g., measured thickness values) for the particular separation distance, h. Therefore the $\gamma(h)$ value quantifies the average squared difference between two values separated by h. A plot of this function for various separation distances allows for the identification of range and sill values (Kitanidis, 1997).

Spatial structure in a dataset is defined by a range, the distance at which the variogram no longer continuously increases, and a sill, which is the value of γ that the data fluctuates around, equal to the variance of *z* (Kitanidis, 1997). Periodicity in a dataset causes the variogram to fluctuate periodically around a sill. Self-affine datasets, such as fault surfaces (Sagy *et al.*, 2007; Candela *et al.*, 2012), should increase continuously across all lags within a data set. However, variograms of synthetic and natural fault core thickness have been shown to demonstrate spatial structure, as the thickness of the fault core has a known maximum value and does not continuously scale (Lunn *et al.*, 2008; Brown and Bruhn, 1996).

Variograms were calculated for the traces of the top and bottom of layer d, the top and bottom of the inner fault core, and the layer d thickness data for individual exposures. Maximum lag for a variogram is half the length of the input data, as the variogram at greater lags is calculated from fewer pairs of data and is less robust (Caers and Zhang, 2004). Histograms of all input data were plotted to test for a normal distribution. Variograms are best calculated on data with a normal distribution, as outliers in a skewed distribution may unduly influence the result. If the distribution was not normal, a log10-transform was performed to reduce the skew in the data (Kerry and Oliver, 2007). The linearly interpolated sections of the combined traces were removed and the vertical difference between each found to create a full extent thickness data set for d. Variograms of the full extent layer d thickness were then calculated. We calculated a variogram of fault core thickness, but this was not included as thickness variograms were used to show characteristic asperity size and the contacts of the inner-outer fault core are not in contact.

In addition to field data, synthetic, self-similar fault traces were also calculated following the method of Dunham *et al.* (2011) to compare these results with natural fault surfaces. In this method, the PSD is calculated in the frequency domain by scaling a random amplitude

distribution by a specific roughness (amplitude/wavelength), and a synthetic trace created by performing an inverse Fourier transform. We used a roughness of 10^{-3} (after Chester *et al.*, 2004). Multiple fault traces (20) were created to use as a control to compare the results of field data analysis and expected results from a fractal surface. These data were subjected to the same variogram analysis as all field data.

The variograms for the upper outer fault core contact show different behavior at each exposure examined (Fig. 2.9). Exposure 1 is fit with a linear model. Exposures 2 and 3 both require a spherical model, though the ranges are different, and the sills of the variograms fluctuate periodically. Exposure 2 has a range of 2.65 m; after this range the sill has a 2 m wavelength sill fluctuation. The model for exposure 3 has a range of 1.14 m with 1 m wavelength sill fluctuation.

The lower outer fault core contact is also fit with a different model at each exposure (Fig. 2.9). Exposure 1 is fit with a linear model. Exposure 2 is fit with a periodic model with a wavelength of 15 m. Exposure 3 requires a spherical model with a range of 1.63 m and 4 m wavelength periodicity around the sill.

Layer d edge variograms for Exposures 1 and 3 demonstrate linear behavior for both the bottom and top contacts of d over all length scales analyzed (Fig. 2.9). Exposure 2 is not clearly fit with a linear model and does show a sill with a range of 6.32 m. A true spherical model is not an ideal fit, however, as the data falls below the sill at longer length scales.

The thickness of layer d fluctuates in a periodic fashion (Fig. 2.10a). Thickness values of this layer show a positively skewed distribution, so we performed a log10-transformation for calculation of the variogram (Appendix D). Variograms of layer d thickness from three

individual exposures are all fit with spherical models, with ranges of 2.51 m, 0.80 m, and 1.91 m (Fig. 2.10b, c, d). The sills all fluctuate periodically, with wavelengths of 3 m, 1 m, and 2 m. The variogram of the complete data set (maximum length of 83.7 m) requires a combination model, with a range of 0.9 m, similar to the ranges from individual exposures, and a periodically fluctuating sill of ~4 m (Fig. 2.10e).

2.4.3 Method limitations

In comparison to recent works on fault geometry, our data set is limited as we analyze single cross sections for each trace. Methods based on terrestrial laser scanner (TLS) point clouds of slickensides consider the entirety of a fault surface and average the power calculated at each frequency over thousands of traces, resulting in representative quantitative analyses (Sagy *et al.*, 2007; Candela *et al.*, 2012). Analysis of a single trace is sensitive to outliers in the overall geometry of a surface. However, the ß values in our results are similar to those derived from surfaces measured in previous studies (Fig. 2.8) (Sagy *et al.*, 2007; Brodsky *et al.*, 2009), suggesting the traces of the inner-outer fault core contacts in cross section analyzed here are equivalent to one slip-perpendicular profile from fault surfaces analyzed using TLS. Additionally, considering a single trace allows us to focus on the details of the geometry that record small scale wear processes that may be averaged out by analyzing multiple traces. The cross-sectional views we utilize also allow comparison of the geometry of multiple surfaces or layers within a single fault core, which is impossible when considering a fault surface.

The cross-sectional views of the fault core are dependent on the trend of the cliff where exposures are uncovered. Exposures trend 17° or less off fault strike, but variation in the exposure trend may account for differing estimates of roughness from exposure-to-exposure (Lee

and Bruhn, 1996; Candela et al., 2012). However, the relative relationships between the layers within each exposure would be unaffected by this and are consistent exposure-to-exposure.

Any model created by PhotoscanPro from a single set of input photos can be slightly different each time a model is created, so we verified the precision of the maps by generating multiple models for one exposure from the same input photos and model parameters (Appendix C). Test traces of the edge of the inner fault core were produced from each model. The PSD for the test traces were extremely similar at length scales of ~10^{-2} m and greater. Noise in the PSD at short length scales suggests small-scale (sub-cm) characteristics of the traces vary slightly between models. However, variability between the test traces was substantially less than the variability between different contacts suggesting the roughness measurements are reliable.

Both the power spectral density and variograms assume ergodicity and stationarity of the data. Stationarity requires that exposure analyzed represents the same population of data, with the same mean, variance and autocorrelation structure. Strict stationarity is nearly impossible to observe in natural systems, but we did test the data for weak stationarity (Appendix D). No combination of exposures for the edges and thickness of the inner-outer fault core contact or layer d were stationary. We suggest that the non-stationarity of the data demonstrates the impact of spatially variable small-scale wear processes on the fault thickness and geometry.

The power spectra of most of the surfaces are continuous over all scales, indicating self-affine contacts, which should result in linear variograms. As not all our variograms were best fit by a linear model, we plotted a variogram of a synthetic self-similar surface to test if the observed periodicity is an artifact (Fig. 2.9). The self-similar surface is best fit with a linear model, which confirms non-linear models are a result of a real signal rather than an edge effect.

The lack of a break in slope in the PSD at the wavelength of periodicity in the variogram may be because the Welch method dampens any break in slope. Slope changes are minimized as the windows are arbitrarily chosen and the signal split into multiple windows in which any periodic wavelength would be out of phase. The slope changes are clearer when the PSD is not smoothed with the Welch method.

2.5. Interpretation and Discussion

2.5.1 Deformation History of the Boyd Fault:

Crosscutting relationships and compositional differences define the deformation history of the Boyd fault, though few absolute timing constraints are available. Three phases of deformation are evident: early ductile deformation, brittle formation of the outer fault core, and brittle formation of the inner fault core.

Both the Asbestos Mountain batholith and Palm Canyon Complex contain foliations and folds that attest to ductile deformation. Foliation in the lower outer fault core (Palm Canyon) has been entirely overprinted by later deformation near the fault (up to ~15 m away). In contrast, upper outer fault foliation is apparent and defined by aligned hornblendes and biotites and is gently folded at the exposure scale. The Asbestos Mountain tonalite regionally contains a weak magmatic grain shape fabric (Morton *et al.*, 2014). We observed an increase in intensity of the foliation towards the fault and a variable attitude, suggesting foliation deflection as a result of an increase in strain associated with the early stage of the fault evolution (Fig. 2.11, phase 1). Available thermochronologic data suggest the ductile deformation occurred from 87 Ma (emplacement of the Asbestos Mountain tonalite) to ~70 Ma when both the hanging wall and footwall cooled through 300° C (Wenk *et al.*, 2000).

Cataclastically deformed Asbestos Mountain tonalite and Palm Canyon Complex, including pseudotachylytes, in the outer fault core crosscut the ductile structures (Fig. 2.11, phase 2). This shows brittle deformation post-dated ductile deformation. At mesoscopic scale in the upper outer fault core, regions of cataclasite entirely overprint the foliation with a sugar-like texture, fine grain size, and aphanitic grains, with no biotite or hornblende (Fig. 2.2a). The lower outer fault core has an entirely cataclastic texture varying in composition along strike as a result of variation in protolith lithology and subsidiary faulting. Epidote, chlorite, actinolite and albite in the outer fault core cataclasites indicate the deformation occurred at greenschist facies conditions (Fig. 2.2a). Pseudotachylyte veins interpreted as reverse-sense in the lower outer fault core appear between and within bands of cataclasite, indicating a synchronous formation. Ages from $^{40}Ar/^{39}Ar$ dating of pseudotachylytes from the outer fault core suggest they formed at 56-62 Ma, ~74 Ma and ~39 Ma (Wenk *et al.*, 2000). These ages are consistent with brittle deformation occurring at lower temperatures than the earlier ductile deformation (Wenk, *et al.*, 2000).

The ultracataclastic inner fault core crosscuts all outer fault core deformation and has a distinct mineralogical composition (Fig. 2.2a, Fig. 2.5, Fig. 2.11 phase 3). Ultracataclasite layers within the inner fault core and normal-sense shear fractures extending from the edge of the inner fault core truncate or offset the foliations, cataclasites, and pseudotachylytes in the outer fault core (Fig. 2.2c, Fig. 2.5, Fig. 2.6). Ultracataclasite layers contain clasts of cataclasite from the outer fault core, but the reverse is not observed (Fig. 2.4). Proportionally large amounts of laumontite and a lack of anorthite suggest a lower temperature of formation in the inner fault core than the outer fault core, as the crystal structure of laumontite is unstable at temperatures above 250° (Fig. 2.2a; Rykl and Pechar, 1984). These observations show deformation associated with the inner fault core occurred post-Laramide (Fig. 2.2b, c). As the pseudotachylytes are

consistently crosscut by the normal shear fractures, which splay from the inner fault core, the inner fault core could have formed during a phase of extensional reactivation during the Miocene (cf. Axen and Fletcher, 1998) The cumulative displacement of the inner fault core is difficult to estimate because of a lack of piercing points or other displacement indicators. Given an average thickness of 22 cm, an approximate slip estimate is around 90 m for the inner fault core (Childs *et al.,* 2009).

Layer d locally truncates all other deformation structures, including the inner-outer fault core contacts, and has the finest grain size of all ultracataclasite layers, indicating it was the last structure to form in the Boyd Fault (Fig. 2.6a, b, c, Fig. 2.11 phase 4)(An and Sammis, 1994). The presence of amorphous material and presence of swelling clay minerals in this layer indicates it formed at a lower temperature than other ultracataclasite layers that contain illite (Moore and Saffer, 2001). Injection veins from layer d that branch up into the hanging wall crosscut all other fault rocks (Fig. 2.6c). Ultracataclasite within the injections and layer d is homogeneous in composition and forms a single coherent unit. A slight foliation is seen in the layer at microscopic scale, but proportions of elements across the layer remain consistent and no localization of shear within the layer is observed, suggesting shear deformation was distributed across the layer (Fig. 2.7g). Foliation in gouge or ultracataclasite material has been observed for experiments simulating creep, but also has been observed at seismic slip rates (Ujiie *et al.*, 2013; French *et al.*, 2014). The injection veins indicate that layer d was fluidized and overpressured due to coseismic shear (Otsuki *et al.*, 2005; Lin, 2011; Rowe *et al.*, 2012).

Layer d is continuous across all five exposures we studied and is present in exposures of the fault over 5 km away from the main study area (Fig. 2.1a), consistent with formation during a moderate-sized earthquake. In some locations, layer d contains clasts of ultracataclasite material

but no other ultracataclasite layers are present. This suggests either this layer entirely overprinted some pre-existing ultracataclasite layer or this layer experienced granular flow during slip. Layer d therefore represents at least one seismic slip event, but potentially many, and the number of events represented by the layer is unknown. The displacement on layer d is unconstrained, though the range on the thickness variogram (1.66 m for layer d) has been previously interpreted to represent shear offset in the fault parallel direction (Brown and Bruhn, 1996). This implies displacement on layer d was significantly greater than 1.66 m, as we examine exposures in the fault perpendicular direction.

2.5.2 Roughness evolution

Our interpretation of the deformation history of the Boyd fault is that the outer fault core formed before the inner fault core and that layer d was the most recently active layer within the inner fault core. We use these relative timing relationships to track the evolution of the geometry over the duration of the deformation.

The roughness measurements show the edges of layer d are notably smoother at all wavelengths than the traces of either the upper or lower inner outer fault core contacts (Fig. 2.8). Previous constraints on smoothing from a compilation of faults suggest a weak trend with displacement (Brodsky *et al.*, 2011). Because layer d is the youngest component of the fault zone, our observations document smoothing of the fault over the duration of deformation for a single fault. As narrow principal slip zones are characteristic of faults in many tectonic settings (*e.g.* Chester and Chester, 1998; Sibson, 2003; Chambon *et al.*, 2006; Sagy and Brodsky, 2009), detectable smoothing of individual faults with displacement may be common.

Layer d represents localization of strain with displacement. However, some characteristics of the inner fault core indicate layer d formed by re-nucleation of a new layer rather than from progressive wear of a pre-existing surface. The inner fault core has up to 12 layers preserved in any given outcrop, indicating new layer formation occurred many times over the duration of displacement, in contrast to geometrically simpler systems where the most recent slip zone accommodated the majority of displacement (Chester and Chester, 1998). Layer d has sharp, clearly defined edges and is oriented slightly differently to other ultracataclasite layers. Consequently, it truncates pre-existing layers at an angle rather than exploiting them or localizing within a thicker gouge layer (Chester and Chester, 1998).

2.5.3 Scale Dependent Wear Processes

In addition to the overall evolution in roughness described above, our observations document distinct wear processes on the Boyd Fault at micron to meter scales that show the trends are a function of a complex set of interrelated processes. We propose that smoothing processes acted in tandem with re-roughening processes, as we observe some processes that smooth at one scale re-roughen the fault surface or slip zone when considered at another scale. This interplay between smoothing and re-roughening processes results in scale-dependent wear of the fault core (Fig. 2.12).

SEM observations of the geometry of layer d contacts show re-roughening occurred at the edge of layer d as a result of grain plucking due to slip distributed across the layer (Fig. 2.12a). Rounded to sub-rounded grains were plucked from the outer fault core and integrated into layer d (Fig. 2.7c). Grain plucking causes the contact between layer d and the outer fault core to roughen because the absence of the grain creates an embayment on the fault surface at the scale

of the plucked grain (Fig. 2.12a). Repeated removal of many grains reduces the amplitudes of asperities larger than the grain size, reducing the roughness of the layer contact at scales greater than the grain size. When layer d is adjacent to the lower outer fault core contact at exposure 1, this contact is smoother at all scales in comparison to the lower outer fault core contact at other exposures. This indicates wear during the formation of layer d, which possibly occurred by grain plucking (Fig. 2.8a, b, c). No clasts are observed to be truncated by layer d at sub-centimeter scale, but layer d does truncate clasts at centimeter scale within adjacent ultracataclasite layers (Fig. 2.6a). We propose this truncation occurred by aggregation of plucked grains from the truncated clast into layer d. The scale of the plucked grains also directly affects the shape of the contact from which they are plucked. The contact between layer d and other ultracataclasite layers (bottom of d at exp. 2 and 3) is smoother than the contact between layer d and the inner-outer fault core contacts (top of d at exp. 2 and 3)(Fig. 2.8b, c). We interpret this to be as a result of smaller grain size and difference in material properties for ultracataclasite in comparison to the outer fault core. This suggests smoothing and localization are complementary processes.

The formation of lenticular clasts within the inner fault core is also representative of a scale-dependent smoothing and re-roughening process (Fig. 2.4; Fig. 2.12b). Microstructural observations show that the aspect ratios of all clasts at sub-centimeter scale are roughly equidimensional (0.8 aspect ratio), indicating lenticular clast formation is unique to centimeter to decimeter scales (although equidimensional clasts exist at all scales). Based on the asymmetric geometry and long axes aligned with the layer edges, we interpret the lenses with a flat edge facing the protolith as asperities that were sheared off from a rough surface. Removing asperities is a process that results in a smoother surface (Fig. 2.12b, left). However, new fracture surfaces are rough (Bouchaud *et al.*, 1990). As the grain-scale plucking described above smoothes

surfaces constantly during displacement, the new fracture surface that forms where a lenticular asperity is sheared off may be rougher than the surrounding surface. This process therefore results in a fault surface that is smoother at scales greater than the lens dimension, but roughening at scales smaller than the lens dimension where the lens was broken off. Shearing off all asperities in the cm to m range as the deformation progresses has an effect comparable to a low pass filter on the surface geometry: the longer wavelengths are smoothed and intermediate wavelengths suppressed (Fig. 2.12c).

Alternatively, when the flat edge is oriented away from the protolith, the formation of the lens occurred as a slip zone splayed from the active layer into adjacent rock at a low angle, surrounding the lens (Fig. 2.12b, right). When this happens, the fault surface is rougher at both centimeter and decimeter scale, as a new fracture surface is locally integrated into the fault surface and the embayment around the lens roughens the surface. Formation of lenticular clasts within a fault core has been observed in multiple locations and at multiple scales (Chester *et al.*, 2004; Cowan *et al.*, 2003; Swanson, 2005). No clear field evidence suggests why these lenticular clasts form, though one potential reason is exploitation of previously existing or syn-kinematic fractures oriented at low angles to the fault. The formation of splays has also previously been linked to adhesion of a slip surface diverting slip onto a new surface, forming a splay.

Aspect ratios of clasts within layer d do not show a constant scaling relationship over all scales of analysis, as microscopic clasts within d are primarily equidimensional. However, lenticular clast aspect ratios show a constant scaling relationship from 3 cm to 90 cm, dependent on material (Fig. 2.4). The PSD show the surfaces we analyzed have self-affine characteristics ($\beta < 3$), meaning they scale differently in the x (fault plane) and z (normal to fault plane) directions (Fig. 2.8). Because lenses were sheared off the layer edge, lenses could reflect the shape of the

surfaces at the time of lens formation. However, a constant aspect ratio suggests a self-similar surface. Our dataset is limited, so we cannot rule out a non-linear scaling relationship, but constant scaling and the range of lengths could imply the lenses reflect a preferred aspect ratio that favors fracturing and lens integration over grinding or more progressive wear. Lenses are not observed above 90 cm in length, indicating lenses above this scale may be mechanically inefficient to produce or alternatively were not observed in the field.

Syn-kinematic displacement on subsidiary fractures that branch from the inner-outer fault core contact (and in some cases layer d) created local spikes in ultracataclasite thickness. Consequently, this is a re-roughening process at centimeter and decimeter scales (Fig. 2.5b, c). Ultracataclasite fills in the space created by conjugate fracture sets, leading to new asperities on the fault surface at decimeter scale. The subsidiary fracture surface, rougher as it has experienced little, is integrated into the fault surface making the surface rougher at centimeter scale.

On power spectral density plots, the upper outer fault core contact is rougher than the lower outer fault core contact over wavelengths less than 2 m, suggesting smoothing of the relatively oldest surfaces we analyzed was spatially discontinuous and scale-dependent over the deformation history (Fig. 2.8). As there is a large accumulation of ultracataclasite in the inner fault core, the different roughness may be due to spatially variable wear dependent on the relative position of slip localization within the ultracataclasite layers. In addition, as the upper contact of the inner fault core is the roughest at every exposure, differences in material properties controlled differing wear rates on opposite sides of the fault.

Several of the variograms of inner-outer fault core contacts are characterized by the presence of sills with periodic fluctuations that reflect a preferred wavelength in a contact (Fig.

2.7). The wavelengths of the sill periodicity for the upper-outer fault core contacts are 2 m for exposure 2 and 1 m for exposure 3. A break in slope of the averaged upper outer fault core PSD occurs at 0.9 m (Fig. 2.8d). This length scale also corresponds with the maximum lens clast length we observed in the field. If this length scale represents the maximum length of lens formation, it may represent a threshold where the fault behaved inelastically below this scale and elastically above. A length scale of ~ 1 m for the crossover from inelastic to elastic strain is a comparable to the value calculated by Kirkpatrick and Brodsky (2014) for the Corona Heights fault. The periodic trace and break in slope in the PSD may therefore reflect inelastic wear of the fault surface eroding the small-scale asperities and altering the fractal characteristics of the fault surface (Fig. 2.12c).

The wavelengths of the sill periodicity for the lower outer fault core contact at exposures 2 and 3 are 15 m and 4 m respectively, but the PSD does not show a break in slope. The upper outer fault core has similar wavelengths of sill periodicity at each exposure (5 and 1 m, 1 m), so calculating power spectral density from multiple exposures emphasizes the 1 m wavelength. In contrast, the lower outer fault core edges show fairly different wavelengths (15 m, 4 m), which may be minimized due to averaging and because 15 m is beyond the maximum length of the PSD calculation.

The top and bottom edges of layer d are fit with linear models at exposures 1 and 3, suggesting the layer has experienced less wear than inner-outer fault core contacts and its original geometry is preserved. Layer d does show evidence of re-roughening processes, such as the splays of ultracataclasite into the upper outer fault core to integrate lenses, but these are not common enough to cause a deviation from a linear model. The variogram of layer d edges at exposure 2 is best fit with a periodic model, indicating the layer is behaving differently within

this exposure. However, at exposure 2, layer d is close to a millimeter thick and its geometry is difficult to resolve in the field maps.

2.5.3.1 Model of evolving fault geometry due to scale-dependent wear:

Overall, our results suggest that the active slip surface within a fault zone switches location within the fault core during deformation as result of strain localization, and that any given surface evolves with displacement. If layer d is representative of this process, the initial shape of the new layer edges would be self-affine over the range wavelengths we have analyzed. Based on the observations of the smoothing and re-roughening processes above, we describe below how layer d would have evolved if the fault had continued to slip (Fig. 2.12d).

Following layer formation, subsequent events may nucleate and crosscut the layer, disrupting layer continuity (Fig. 2.12d1, 2). Wear at the edge of the active slip layer occurs by a combination of cumulative grain plucking at sub-centimeter scales and asperity slicing at centimeter to decimeter scales, resulting in smoother contacts in comparison to the previous slip event (Fig. 2.12a, b, Fig. 2.12d2). As displacement accumulates, complex crosscutting relationships may result as more new layers are generated, truncating lens clasts generated in earlier slip events, injecting ultracataclasite into the outer fault core, and continuing to progressively wear the inner-outer fault core contacts (Fig. 2.12d3). As wear material is generated in the fault, some is integrated into the newest layer by grain plucking while the rest is truncated by the most recent slip event. Generation of wear material results in spatially discontinuous wear of the inner-outer fault core contacts, as they are now deformed by later slip events that may localize on one side of the fault only. Scale-dependent wear processes may have modified asperities below the inelastic-elastic transition (~1 m), resulting in periodic inner-outer

fault core contacts. Relatively new slip surfaces will be self-affine and comparatively smooth as they have experienced little displacement (Fig. 2.12d4).

2.5.4 Definition of an asperity:

Wear processes on fault surfaces are one consequence of the interaction between asperities on opposing sides of a slip zone. Asperity height can be defined as the average deviation of a fault surface from the mean plane through the surface (Archard, 1953). However, many definitions of asperity exist in literature – the definition largely depends on the scale of observation and function of the work. Seismological asperities are regions of a fault surface that experience high dynamic moment-density release during an earthquake (Lay and Kanamori, 1981). Alternatively, assuming fault rock has negligible stiffness compared to the surrounding material, the maximum wavelength of apertures between the two sides of a fault is a representative characteristic length for the fault (Ohnaka, 2013). Scholz (1988) argued this characteristic length reflects the closing of long-wavelength apertures in the fault zone; all wavelengths above the characteristic length will be closed while the shorter wavelength apertures may not be.

On the Boyd fault, we can define the asperity size of the last slip event from the thickness fluctuations of layer d, which is characterized by a periodic variogram (Fig. 2.10; Brown and Bruhn, 1996; Lunn *et al.*, 2008). As the range of the variogram and wavelength for the sill periodicity for each individual exposure are quite close – at exposure 1, the range is 2.51 m with a 3 m wavelength; exposure 2 a 0.8 m range and 1 m wavelength; and exposure 2 a 1.9 m range and 2 m wavelength– these may represent the same physical property for layer d. These thickness fluctuations are also apparent in a map layer of d (Fig. 2.10). The range of the

variograms has been interpreted as representative of the length scale of variability within the fault core due to the shear offset of the fault, assuming that the surfaces were initially well-matched (Brown and Bruhn, 1996). We do not know the original degree of mismatch, but the range and wavelength represent the distance between two points where the thickness of d is negligible. We infer that areas of thin or negligible thickness represent the areas where the sides of the slip zone are in effectively in contact (Nielsen *et al.*, 2010). A length of ~3 m at exposure 1 defines the length scale of spatial continuity in the layer d thickness, which we interpret to be the characteristic wavelength for asperities on layer d at this exposure. Beyond this length scale, opposing sides of the fault are well matched. Variation from exposure-to-exposure in characteristic wavelength of the asperities of layer d may be due to material differences in the ultracataclasite present at each exposure, as the immediate "hanging wall" and "footwall" to layer d changes along strike (either inner fault core or outer fault core). However, asperities of the order of 1 m would be consistent with other estimates from surface geometry (Kirkpatrick and Brodsky, 2014) and with values inferred seismologically (Bouchon *et al.*, 1998, Ide and Takeo, 1997; Mikumo *et al.*, 2002).

2.6. Conclusions

Examination of a single ultracataclasite layer and an entire fault core shows that newly formed fault surfaces are smoother while older surfaces are rougher as a result of wear. Smoothing and re-roughening processes that alter the older surfaces geometry are always paired, as processes that roughen at one scale smooth at another. Periodic fault traces result from these processes, as smaller-wavelength asperities on the fault surface are worn away. Thickness variograms show fluctuations that define the characteristic asperity size for that slip zone.

Table 2.1: Slopes, ß, of the PSD traces for exp. 1, 2, and 3 as well as the 167 m traces over all wavelengths, over the small wavelengths, and over long wavelengths. Numbers in parentheses in the header indicate the range of wavelengths over which the slope was calculated. The plus/minus shows the uncertainty of each slope calculation.

Contact	Exp. 1: (0.05, 11)	Exp. 2: (0.05, 11)	Exp. 3: (0,05, 11)	All: (0.05,11)	All: (0.05,0.9)	All: (0.9,11)
Upper outer fault core	2.82±3.2 e-05	2.47±4.3 e-04	2.57±2.7 e-04	2.33±1.2 e-04	2.60±7.9 e-03	1.43 ±2.3 e-04
Lower outer fault core	2.56±1.1 e-04	2.50±1.4 e-04	2.89±1.3 e-05	2.48±1.6 e-04	2.53±1.1 e-02	2.30±2.8 e-04
Upper layer d	2.41±7.5 e-04	2.31±1.5 e-05	2.70±1.4 e-04	2.11±6.8 e-05	2.14±9.9 e-05	2.35±6.0 e-02
Lower layer d	2.57±3.4 e-04	2.69±2.1 e-04	2.61±1.2 e-04	2.16±1.8 e-04	2.15±9.0 e-03	2.12±2.7 e-01

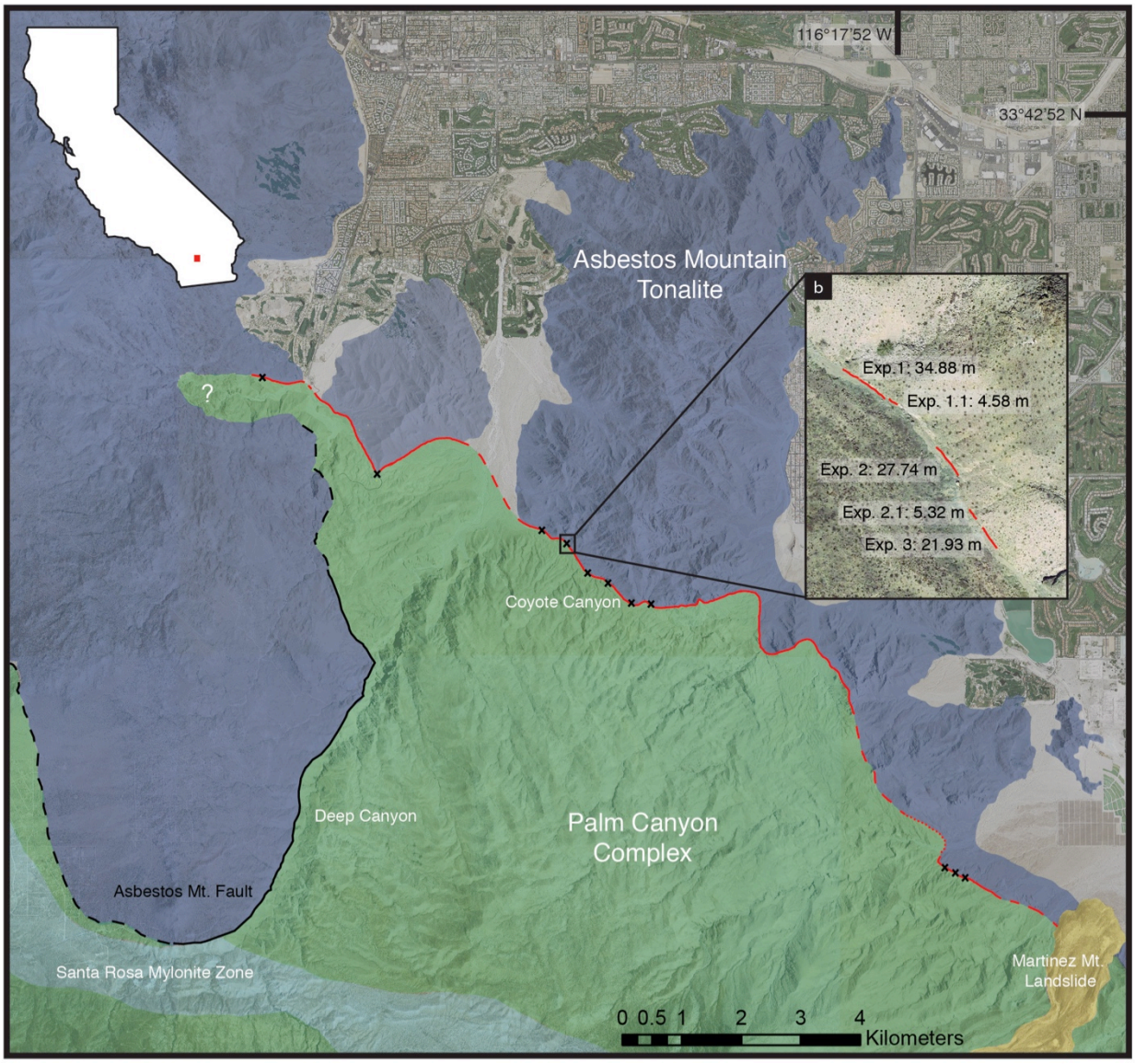

Figure 2.1. Location map: a: Map showing the location of the Boyd Fault in the Eastern Peninsular Ranges of southern California (fault shown by the red line; solid where location is known, dashed where inferred). Crosses show locations where the characteristic internal geometry defined by the presence of layer d is exposed. Solid and dashed black line shows the location of the Asbestos Mountain Fault. Geology modified from Sharp (1979), Wenk *et al*. (2000) White (2006) and Matti *et al*. (2006). Inset California outline shows the location of the field area in red. b: Inset shows in detail the five exposures mapped for analysis. Total length from exposure 1 to exposure 3 is 167 m.

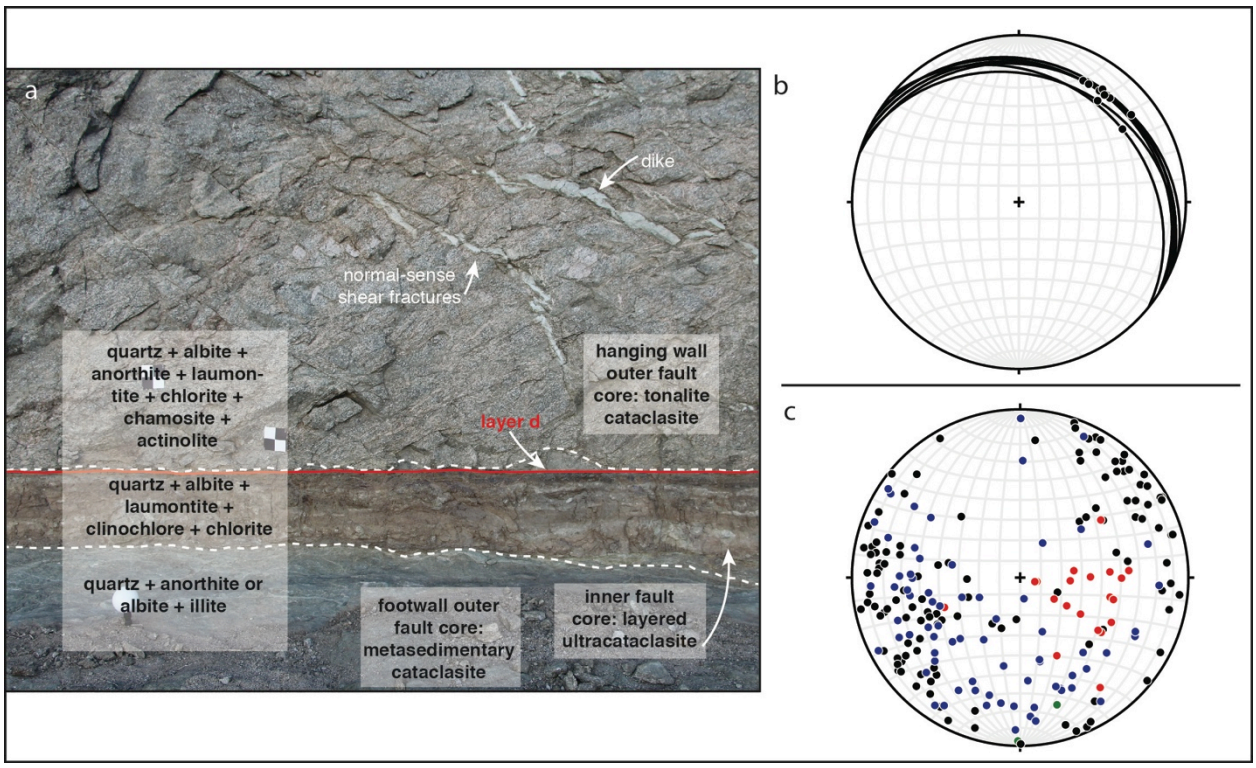

Figure 2.2. Architecture of the Boyd Fault: a: field photograph demonstrating the complex internal architecture of the Boyd Fault. View is approximately in the down-dip direction to the NNE. Layer d is identified with the red line, the white lines show the boundaries of the inner fault core, and the bull's-eye shows the sense of slip (into the page). The general mineral assemblage from XRD for the upper outer, inner, and lower outer fault core is listed on the left. b: fault orientation data measured at 14 locations along strike with the trend and plunge of the lineation of slickenlines on exposed fault surfaces. c: Poles to shear fractures in the upper outer fault core (blue), shear fractures in the damage zone (black) and pseudotachylytes in the damage zone (red).

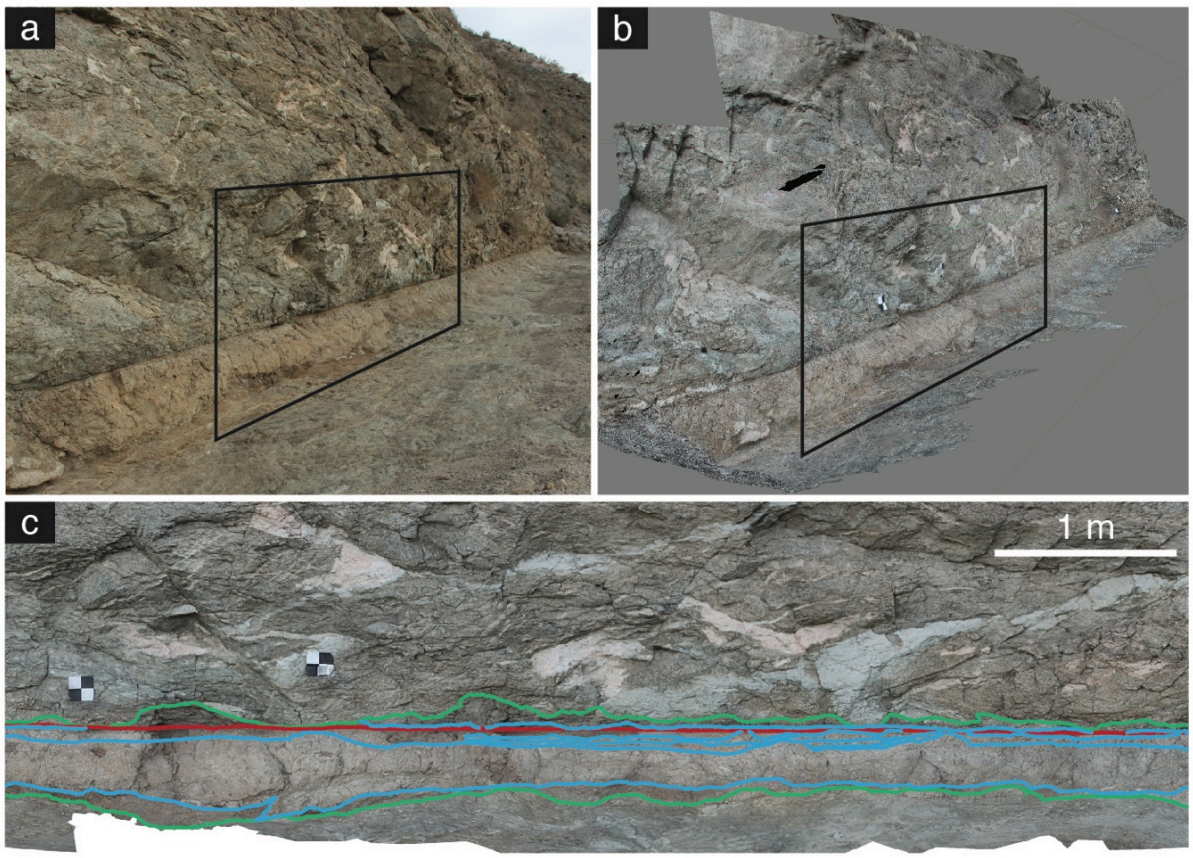

Figure 2.3. Outcrop to field map workflow: a: Oblique photograph of Exposure 3. Around 150 photos similar to this were used to construct the outcrop model. b: Model generated with Agisoft's PhotoscanPro shown from the same perspective as a. Boxes in a and b show the extent of c. c: Orthorectified photograph exported after the model was rotated to view the exposure in the orientation down the slip vector. Lines show traces mapped in the field that were used to calculate roughness. Red lines are layer d, green lines define the extent of the inner fault core, and blue lines show layers within the inner fault core.

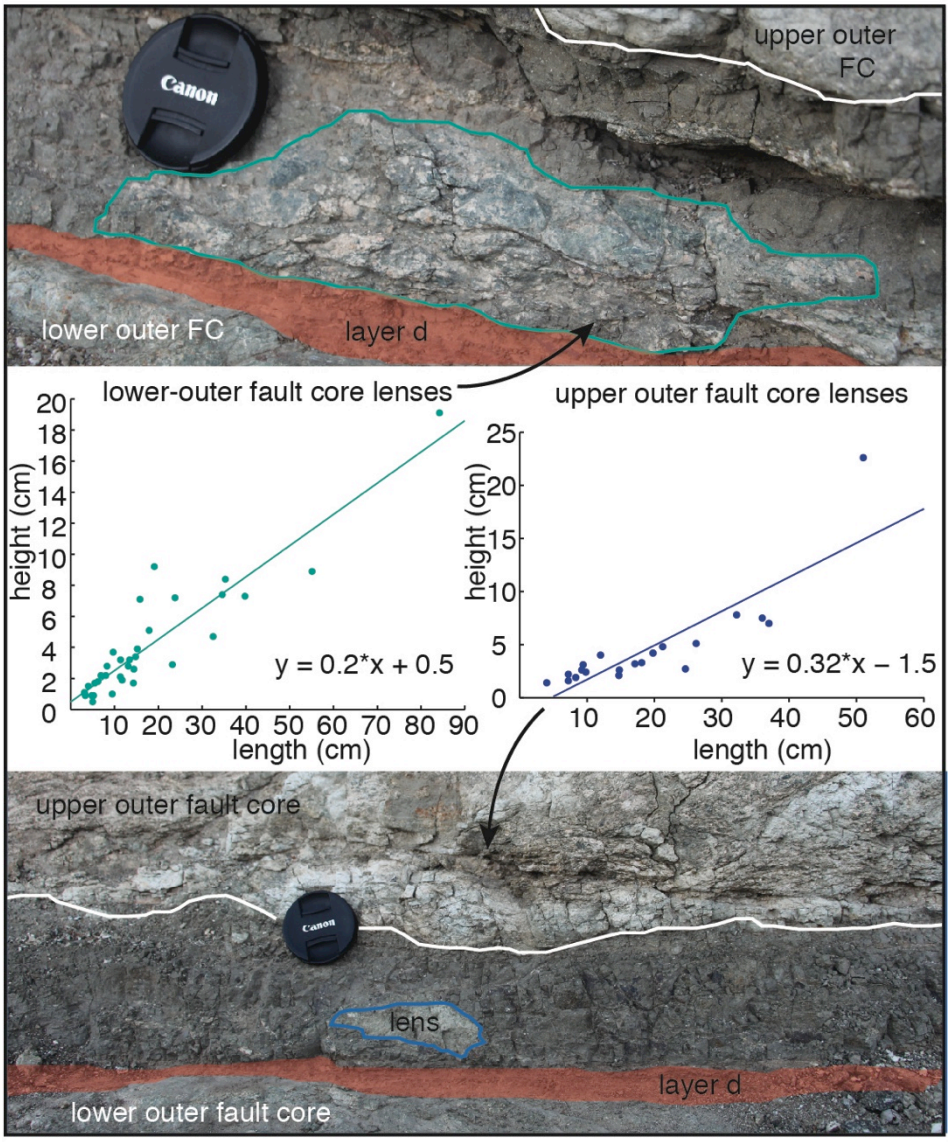

Figure 2.4. Lenticular clasts in the inner fault core. The top photograph shows an example of a lenticular clast from lower outer fault core material in the inner fault core. The bottom photograph shows an example from the upper-outer fault core in the inner fault core. The corresponding plots of aspect ratios of the lenses are in the middle. Each is fit with a best-fit linear model and the slope represents the aspect ratio for that material.

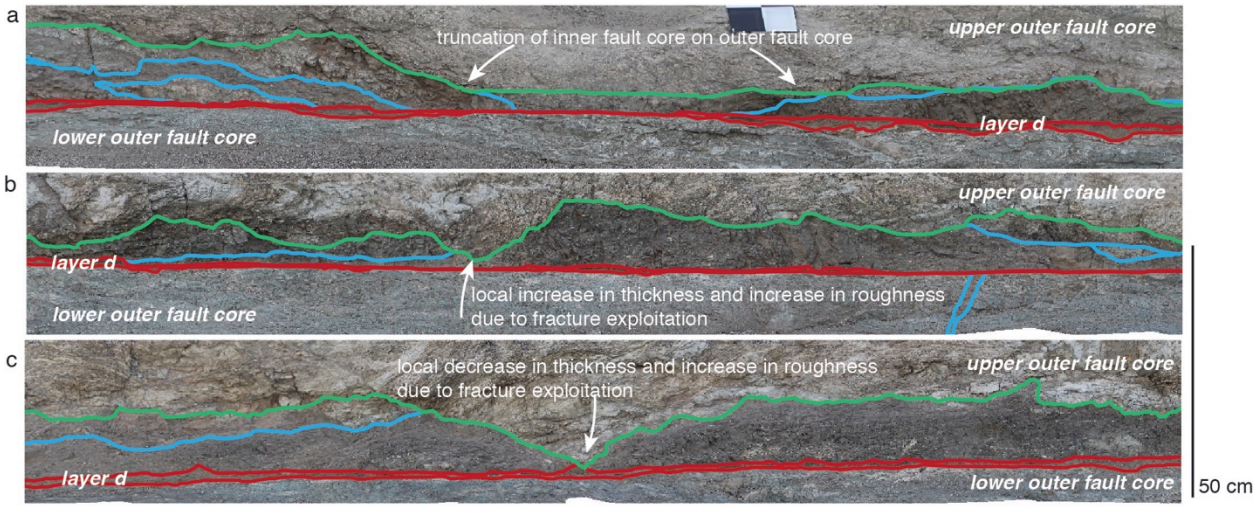

Figure 2.5. Field observations from mapped exposures. Green lines are inner-outer fault core contacts, blue lines are ultracataclasite inner fault core layers, and red lines are layer d. a: layers of ultracataclasite are truncated by upper outer fault core material, while layer d is continuous across the base of the fault core. b and c: the fault core increases locally in thickness due to the exploitation of fractures in the outer fault core.

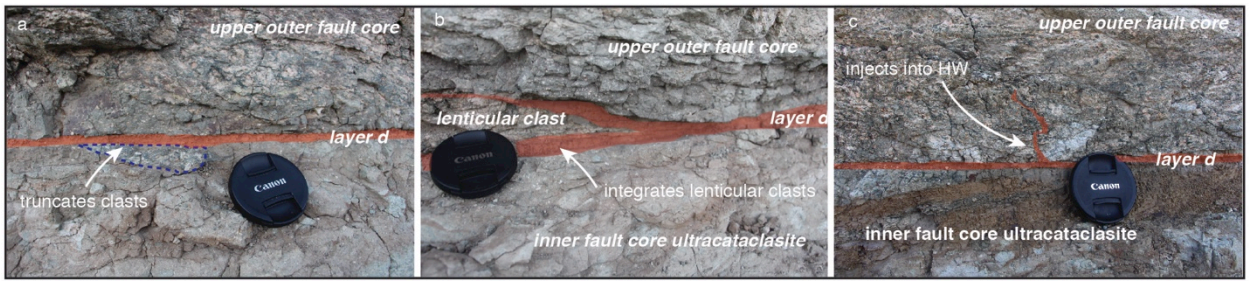

Fig. 2.6. a: layer d (in red) truncates a large clast within another inner fault core layer (camera lens for scale ~6 cm diameter). b: layer d splays into the upper outer fault core to integrate a lenticular clast of outer fault core material, locally increasing its thickness. c: Photograph showing details of layer d (highlighted in red), which injects into hanging wall and also crosscuts layers in the inner fault core (below the red layer).

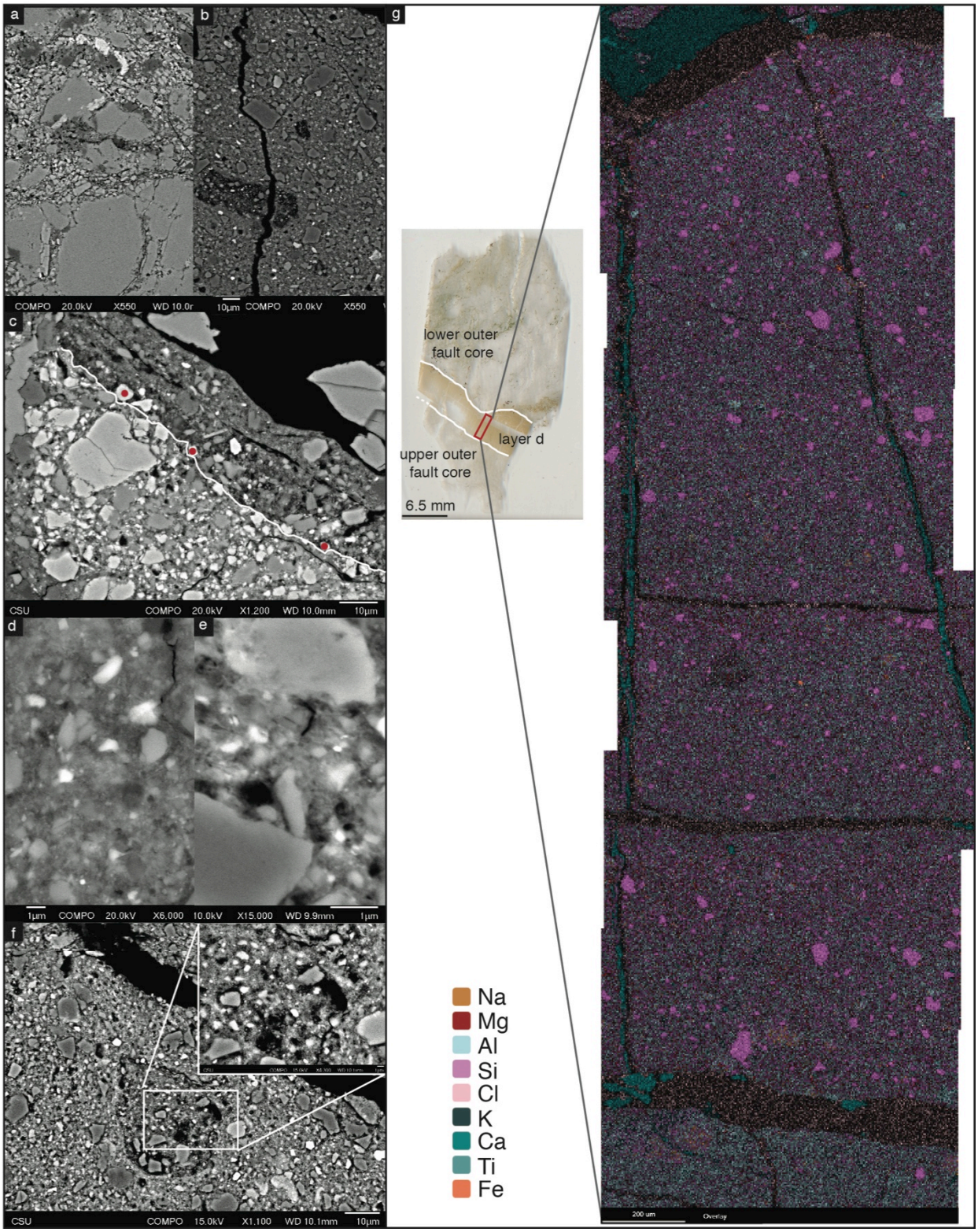
a
b
g
COMPO 20.0kV X550 WD 10.0r
10µm COMPO 20.0kV X550
c
lower outer
fault core
layer d
upper outer
fault core
6.5 mm
CSU COMPO 20.0kV X1,200 WD 10.0mm 10µm
d
e
1µm COMPO 20.0kV X6,000 10.0kV X15,000 WD 9.9mm 1µm
f
CSU COMPO 15.0kV X1,100 WD 10.1mm 10µm
Na
Mg
Al
Si
Cl
K
Ca
Ti
Fe
200 um
Overlay

Figure 2.7 (previous page). SEM and EDS observations: a: SEM image of the upper-outer fault core. Note frequent clasts and larger clast size when compared to b, layer d at the same scale. b: SEM image of the matrix texture of layer d. The rectangular clast within the layer is composed of ultracataclasite. c: The contact between layer d and the upper outer fault core is shown. Grains within layer d marked with a red circle have been inferred as plucked from the upper outer fault core (light). d/e: The matrix of layer d at high magnification, showing clasts are sub-angular to angular and exist at smaller than micron scale. f: Layer d has clasts of other layers of ultracataclasite. The inset shows the texture of the ultracataclasite clast. g: EDS transect across layer d from the upper outer fault core to the lower outer fault core. The legend shows the present elements and their corresponding colors.

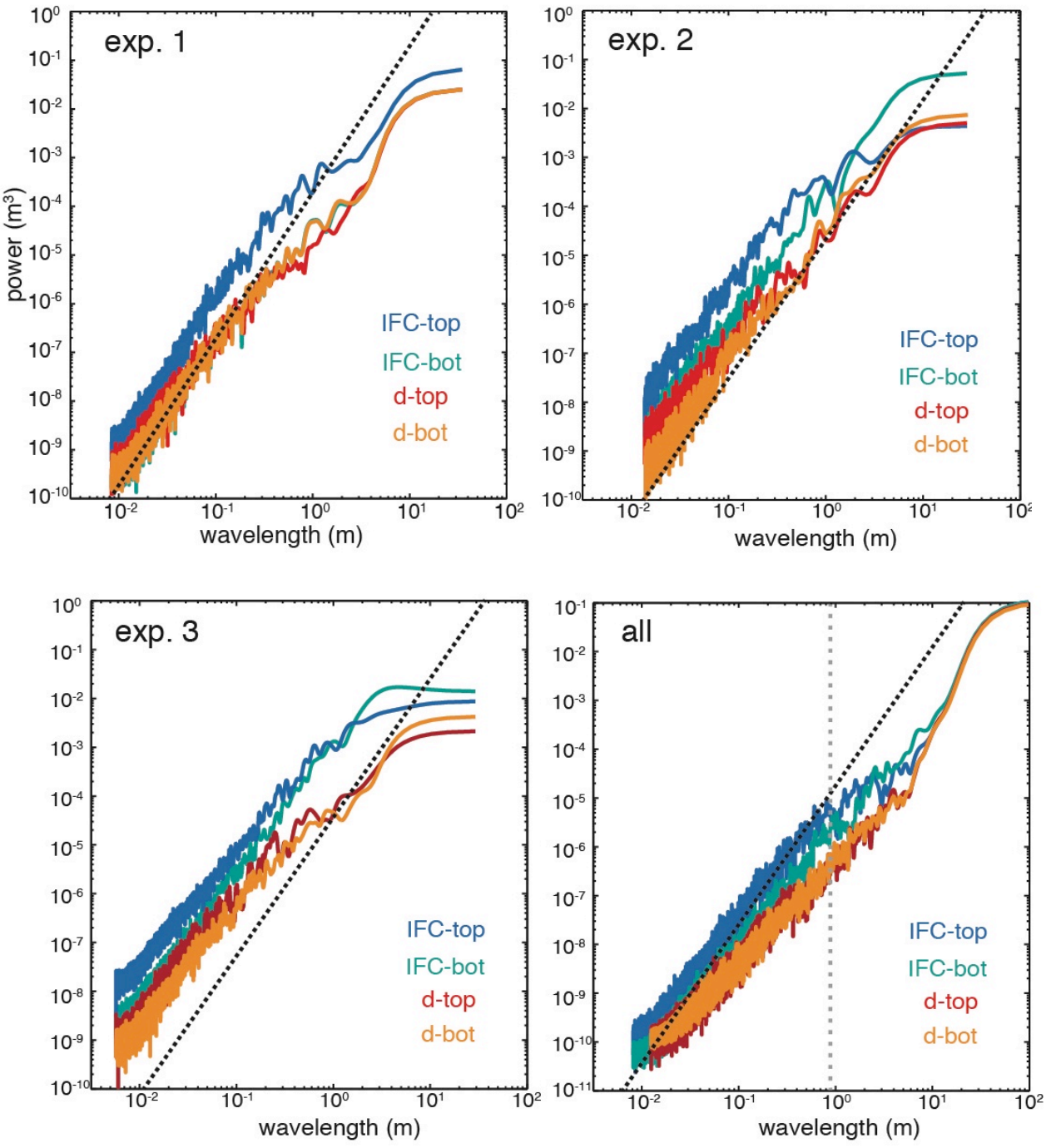

Figure 2.8. PSD from individual exposures (a-c) and averaged across all exposures (d) from layer d and inner-outer fault core contacts. The black dotted line is a reference line with a slope of 3. The gray dotted line for the combined exposure dataset is a reference line indicating the break in slope. Note layer d is smoother at all exposures. The lower outer fault core contact is also always smoother than the upper outer fault core contact.

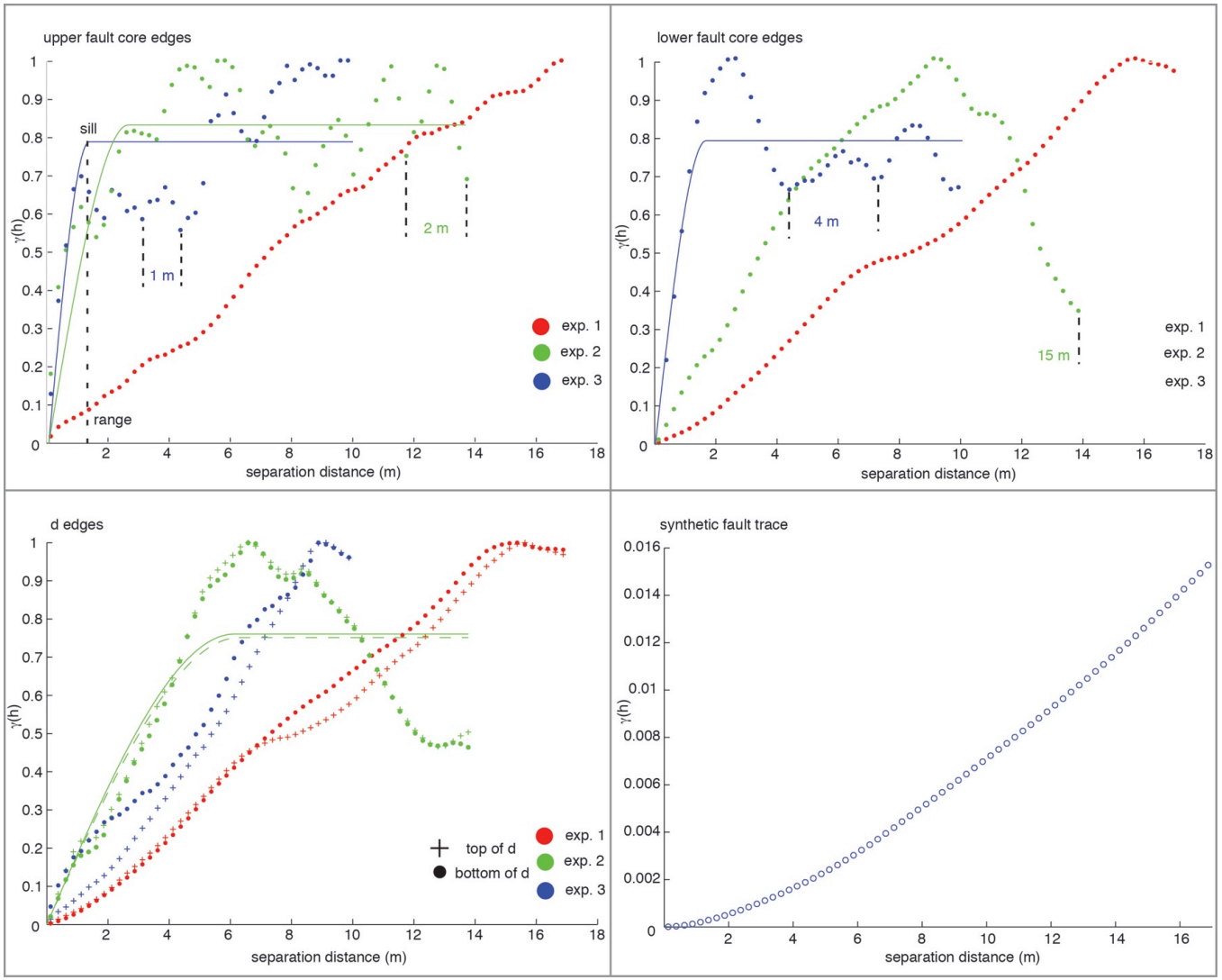
upper fault core edges
sill
range
1 m
2 m
exp. 1
exp. 2
exp. 3
γ(h)
separation distance (m)
lower fault core edges
4 m
15 m
exp. 1
exp. 2
exp. 3
separation distance (m)
d edges
top of d
bottom of d
exp. 1
exp. 2
exp. 3
separation distance (m)
synthetic fault trace
separation distance (m)

Figure 2.9. (previous page). Variograms of the upper-outer fault core contacts (a), the lower-outer fault core contacts (b), the edges of layer d (c) and a synthetic surface (d). Data in a, b, and c are normalized so all exposures could be plotted on the same graph. Variograms are fit with a reference line for their best-fit model if applicable; the color of the line matches the variogram it is modeling.

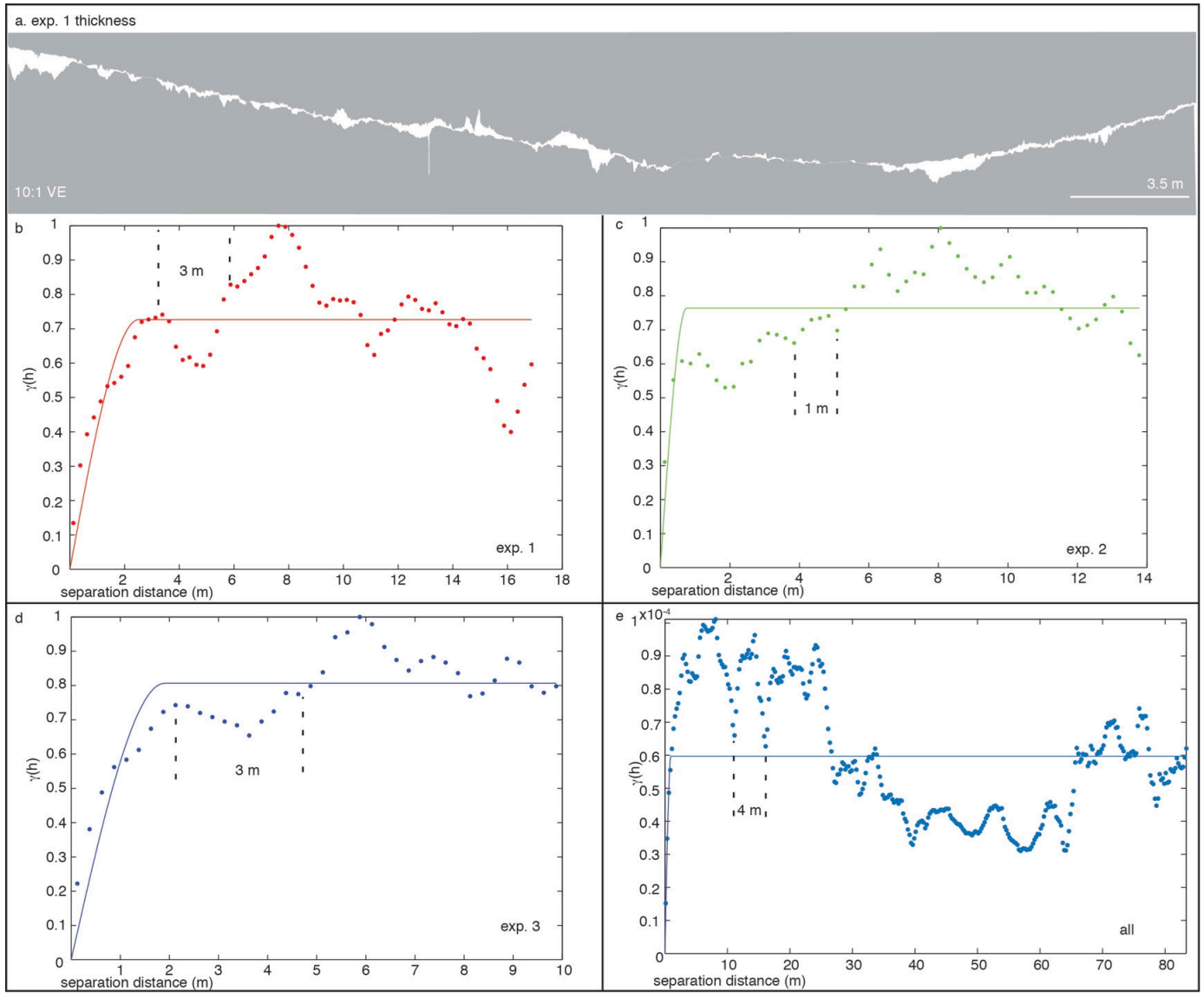
a. exp. 1 thickness
10:1 VE
3.5 m
b
3 m
γ(h)
separation distance (m)
exp. 1
c
1 m
γ(h)
separation distance (m)
exp. 2
d
3 m
γ(h)
separation distance (m)
exp. 3
e
x10-4
4 m
γ(h)
separation distance (m)
all

Figure 2.10 (previous page). Thickness of layer d. a: Map of layer d thickness at exposure 1 with 10:1 vertical exaggeration. b, c, d: normalized thickness variograms calculated for individual exposures of layer d. Best-fit spherical models are shown. e: thickness variogram calculated for the combined dataset. Best-fit spherical model is shown.

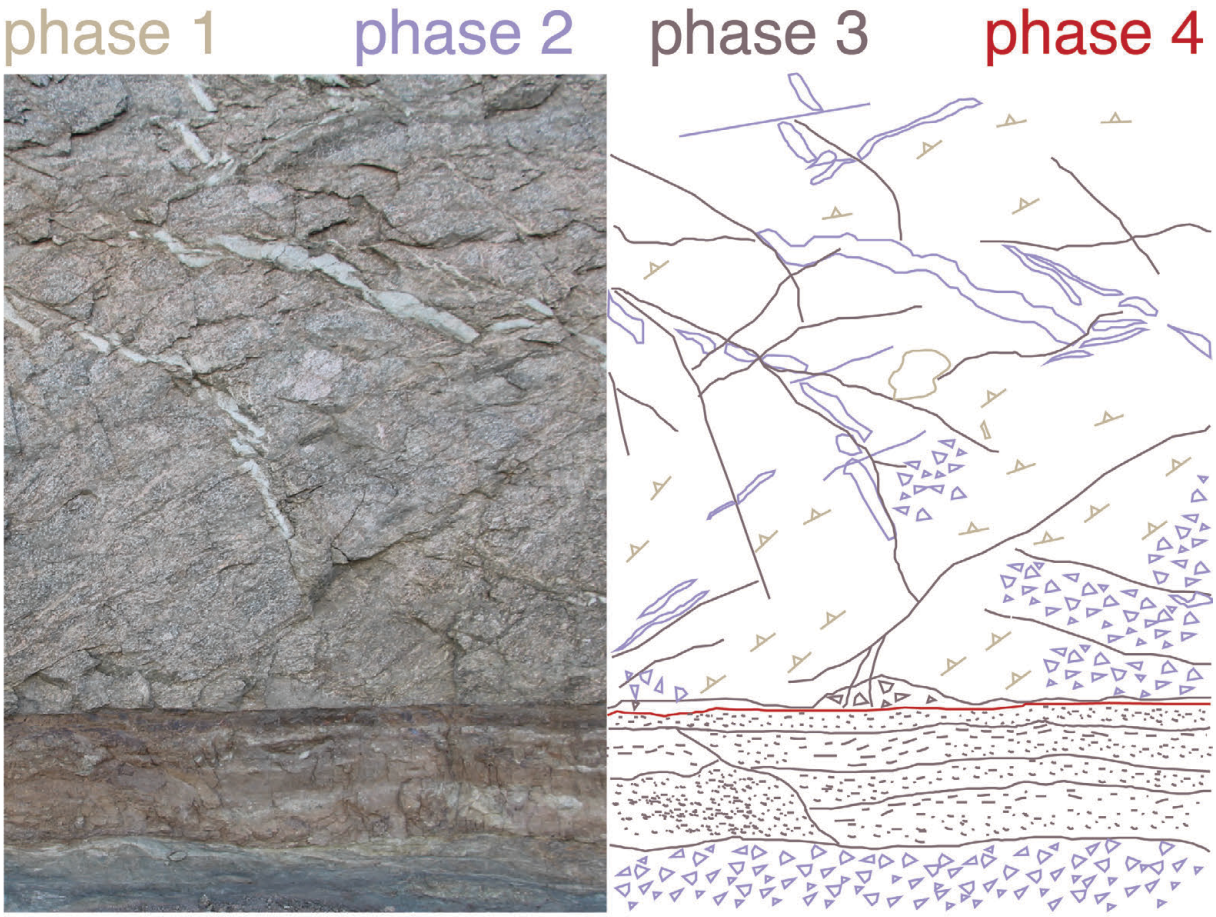

Figure 2.11. Interpretation of the deformation history of the Boyd Fault. The left photograph shows a photograph of exposure 2. The right map shows the different mapped structures and their crosscutting relationships used to develop the phases of deformation during the deformation history of the fault. The first phase is in tan and includes foliations and some dikes. The second phase is brittle, shown in purple, and includes cataclasis (triangles), dikes, and some reverse-sense fractures. The third phase is brown, another brittle phase resulting in the inner fault core and associated normal sense fractures. The final phase is red, the formation of layer d, which crosscuts all other layers. This does not include all evidence of deformation seen near the fault, notably not showing pseudotachylytes which are interpreted to have formed during phase 2.

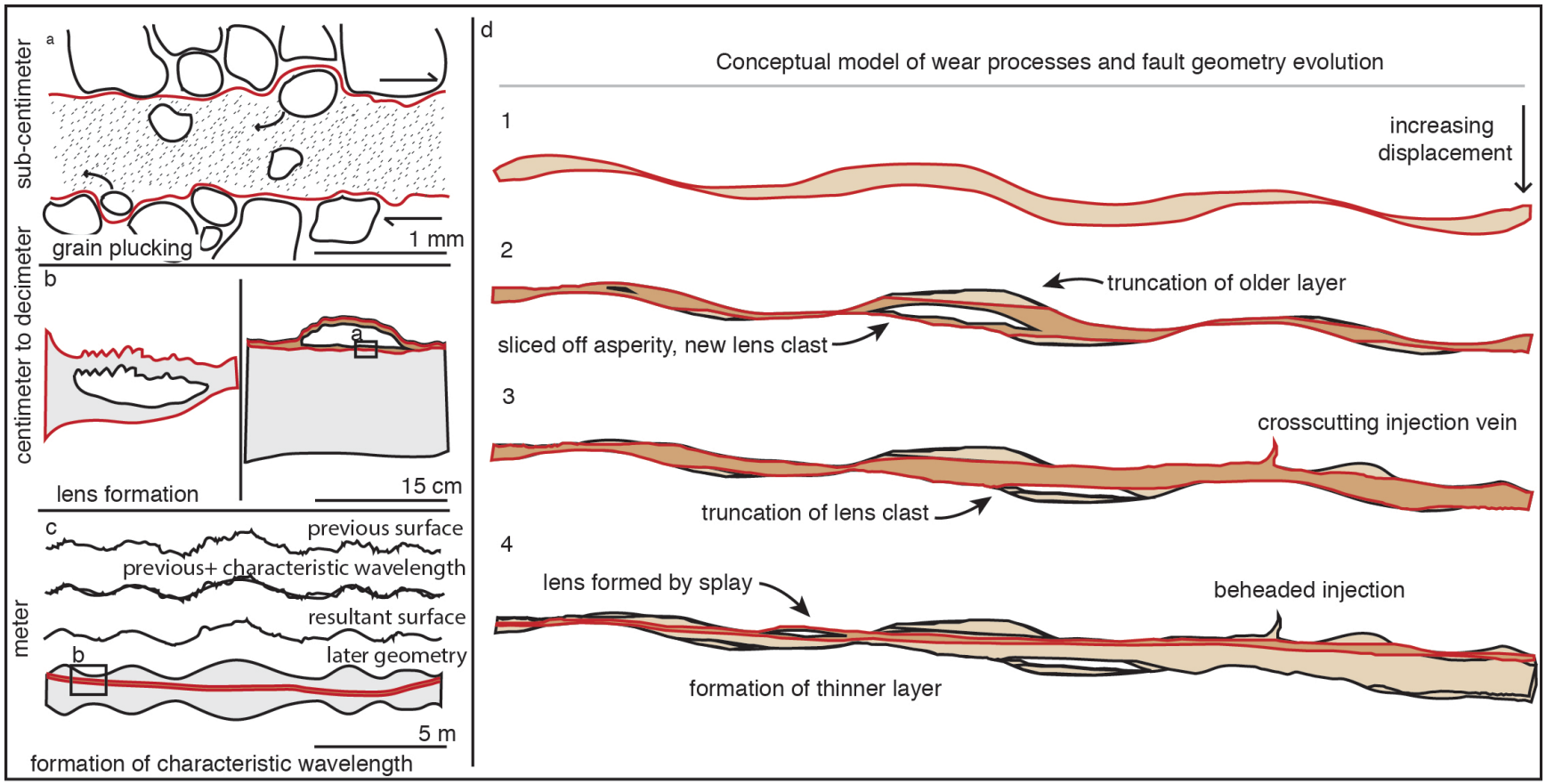

Figure 2.12. Discussion schematic: red lines show active slip surfaces. a: grain plucking at sub-centimeter scale re-roughens the surface at this scale. b: lens formation results in locally rougher surfaces. c: The original, self-affine surface evolves to a periodic surface due to scale-dependent wear. d: Schematic of evolving fault geometry due to scale-dependent wear. With increasing displacement, layers are truncated or overprinted entirely, injections show cross-cutting relations, lenses are formed, and slip localizes abruptly onto a new single surface rather than progressively wearing down a slip surface.

Chapter 3: Future work

Work on the Boyd Fault

The Boyd Fault has not been previously studied in detail, so much of its deformation history has been interpreted from field relationships and limited absolute dates from thermochronological analysis of relatively proximal structures. I have interpreted the inner and outer fault core to have formed in different eras (Laramide and post-Laramide). However, thermochronological analysis of the Boyd Fault would significantly constrain the deformation history and additionally allow us to link – or not link – the deformation on the Boyd Fault to the tectonics of the surrounding region. I found illite and another amorphous clay mineral within the inner fault core, which may be dated by $^{40}Ar/^{39}Ar$ methods though these may produce a variety of ages (Clauer *et al.*, 2012).

I only examined the Boyd Fault geometry from the slip perpendicular direction. Previous work has shown that faults are smoother in the slip parallel direction, so we can assume the fault will be smoother in this direction (Power *et al.*, 1987). However, variogram analysis in the slip parallel direction may be interesting, as we could investigate whether the "wear signature" of periodic behavior would hold true when considered at a different angle. Limited slip parallel exposures exist for the Boyd Fault and they are relatively short, so we would only be able to examine 2-3 m beyond the range of the presented data.

Matti *et al.* (2006) mapped the Boyd Fault (referred to as the La Quinta Fault) as inferred as continuous ~20 km south of the Martinez Mountain Landslide. Other work has detailed extensive normal faulting in Martinez Canyon and Sheep Canyon, roughly along the projected trace of the Boyd Fault (White, 2006). Visiting locations on these maps and characterizing the

internal geometry may extend the length of the Boyd Fault and as a result, the estimated total displacement on the fault.

Grain size reduction has been shown to occur with increased displacement on faults and grain size has a fractal distribution (An and Sammis, 1994). As the Boyd Fault has up to 12 layers at points within a single exposure, this is an ideal way to characterize the deformation history of the fault and investigate the crosscutting relationships within the inner fault core, something that was not considered for this work.

Formation of lenticular clasts due to splays requires low-angle injections of ultracataclasite material to form while the fault is slipping. Generally, injection veins are observed to be oriented at a high angle to the fault plane (Rowe *et al.*, 2012). However, the formation of lenticular clasts as a decimeter-scale re-roughening process requires low angle splays. Additionally, low-angle veins filled with ultracataclasite are also seen on the Boyd Fault. The mechanism behind this is unclear, though veins may exploit pre-existing fractures in the outer fault core. Careful investigation of the field characteristics of these veins is important to understanding the mechanism behind this re-roughening process.

General future work

Experimental work demonstrating the scale-dependence of wear processes and the dependence of wear rate on normal stress have been conducted previously (Boneh *et al.*, 2013; Davidesko *et al.*, 2014). In addition, experiments simulating rough fault geometry have also been conducted (Anthony and Marone, 2005). Simulating variable wear rate on a rough fault surface would be useful to investigate scale-dependent processes and their impact on evolving fault geometry.

Anthony and Marone (2005) show a difference in fault behavior when clasts inside the fault are rounded or angular. Force chains of angular grains form, strengthening the fault. However, what we observe in thin section of layer d is angular matrix grains with sub-rounded to rounded clasts. Simulated fault behavior may change as a result, because force chains could be interrupted by the presence of rounder clasts, weakening the fault and making it more likely to slip.

The wear signature identified on the upper-outer fault core trace is likely identifiable because we studied a single trace. Periodic behavior is likely also observed on other fault traces and is not a characteristic of just the Boyd Fault. Comparison of multiple, randomly selected slip-perpendicular traces from LiDAR scans of fault surfaces with the geometry of the Boyd Fault using variogram analysis would be a simple way to confirm this. The Punchbowl Fault is also exposed in cross-section, though the cross-section is slip parallel. The Punchbowl has a similar geometry to the Boyd Fault, but the slip zone equivalent to layer d has been interpreted to accommodate a majority of the ~20 km slip on the fault and few ultracataclasite layers exist. A comparison of the geometry of a slip zone thought to accommodate a large amount of slip in comparison to one that represents the fault at its most mature, but likely accommodated relatively little slip, would be a way to further investigate the evolution of slip zone geometry. Additionally, comparison of the fault core contacts of the Punchbowl with the inner-outer fault core contacts of d would be a way to compare the wear signature of different types of fault systems.

Numerical modeling of seismic slip on non-planar faults is key to describing the dynamics of rupture propagation and resultant ground motion (Dunham *et al.*, 2011). Models are based on real fault geometries and expected strength of rocks, but do not integrate the presence

of ultracataclasite or other fault-related material between the two sides of the fault. The presence of ultracataclasite may affect the behavior of the fault during slip, as it is fairly weak in comparison to intact rock. In addition, layer d is generally flanked by ultracataclasite. Mature faults, with a large accumulation of fault material, may be rupturing in weak fault related material rather than stronger, intact rock. Simulating rupture in weaker material to compare to intact material would be a way to investigate the role of ultracataclasite during slip.

References

Aki, K. (1984), Asperities, barriers, characteristic earthquakes and strong motion prediction: J. Geophys. Res., 89, 5867–5872, doi: 10.1029/JB089iB07p05867.

An, L.J. and C.G. Sammis (1994), Particle size distribution of cataclastic fault materials from southern California: a 3-D study, Pure Apply. Geophys., 143, 203-227.

Anthony, J. L., and C. Marone (2005), Influence of particle characteristics on granular friction, J. Geophys. Res., 110, B08409, doi:10.1029/2004JB003399.

Archard, J.F. (1953), Contact rubbing of flat surfaces, J. Appl. Phys. 24, 981–988, doi: 10.1063/1.1721448.

Armstrong, R.L., and J. Suppe (1973), Potassium–argon geochronometry of Mesozoic igneous rocks in Nevada, Utah and southern California, Geol. Soc. Am. Bull. 84, 1375–1392, doi: 10.1130/0016-7606.

Axen, G.J. and J.M. Fletcher (1998), Late Miocene-Pleistocene extensional faulting, northern Gulf of California, Mexico and Salton Trough, California, Int. Geol. Rev. 40, 217–244, doi: 10.1080/00206819809465207.

Bistacchi, A., W.A. Griffith, S.A.F. Smith, G. Di Toro, R. Jones, and S. Nielsen (2011), Fault roughness at seismogenic depths from LIDAR and photogrammetric analysis, Pure Appl. Geophys., 168, 2345-2363, doi: 10.1007/s00024-011-0301-7.

Boneh, Y., A. Sagy, and Z. Reches (2013), Frictional strength and wear-rate of carbonate faults during high-velocity, steady-state sliding, Earth Planet. Sci. Lett. 381, 127-137, doi: 10.1016/j.epsl.2013.08.050.

Boneh, Y., J.C. Chang, D.A. Lockner, and Z. Reches (2014), Evolution of wear and friction along experimental faults, Pure Appl. Geophys., 171(11), 3125-3141, doi: 10.1007/s00024-014-0801-3.

Bouchaud, E., G. Lapasset, and J. Planes, (1990), Fractal dimension of fractured surfaces: a universal value?, Europhys. Lett., 13, 73, doi:10.1209/0295-5075/13/1/013.

Bouchon, M., M. Campillo, and F. Cotton (1998), Stress field associated with the rupture of the 1992 Landers, California, earthquake and its implications concerning the fault strength at the onset of the earthquake, J. Geophys. Res., 103(B9), 21091–21097, doi:10.1029/98JB01982.

Brodsky, E.E., and H. Kanamori (2001), Elastohydrodynamic lubrication of faults, J. Geophys. Res., 106, 16,357-16,374, doi:10.1029/2001JB000430.

Brodsky, E.E., J.J. Gilchrist, A. Sagy, and C. Collettini (2011), Faults smooth gradually as a function of slip, Earth Planet. Sci. Lett., 302, 185-193, doi: 10.1016/j.epsl.2010.12.010.

Brown, S.R. and C.H. Scholz (1985), Closure of random elastic surfaces in contact, J. Geophys. Res., 90 (B7), 5531-5545, doi: 10.1029/JB090iB07p05531.

Brown, S.R. and R.L. Bruhn (1996), Formation of voids and veins during faulting, J. Struct. Geo., 18(5), 657-671, doi:10.1016/S0191-8141(96)80031-9.

Byerlee, J. (1978), Friction of rocks, Pure Appl. Geophys., 116, 615-626, doi: 10.1007/BF00876528.

Caers, J. and T. Zhang (2004), Multiple-point Geostatistics: A Quantitative Vehicle for Integrating Geologic Analogs into Multiple Reservoir Models, *in* Integration of outcrop and modern analogs in reservoir modeling: AAPG Memoir 80, p. 383-394.

Candela, T., F. Renard, M. Bouchon, D. Marsan, J. Schmittbuhl, and C. Voisin (2009), Characterization of fault roughness at various scales: implications of three-dimensional high resolution topography measurements, Pure Appl. Geophys., 166, doi 10.1007/s00024-009-0521-2.

Candela, T., F. Renard, Y. Klinger, K. Mair, J. Schmittbuhl, and E.E. Brodsky, (2012), Roughness of fault surfaces over nine decades of length scales, J. Geophys. Res., 117, B08409, doi: 10.1029/2011JB009041.

Chambon, G., J. Schmittbuhl, A. Corfdir, N. Orellana, M. Diraison, and Y. Geraud, (2006), The thickness of faults: From laboratory experiments to field scale observations, Tectonophys., 426, 77-94, doi: 10.1016/j.tecto.2006.02.014.

Chester, F.M., and J.S. Chester (1998), Ultracataclasite structure and friction processes of the Punchbowl fault, San Andreas system, California, Tectonophys., 295, 199-221, doi:10.1016/S0040-1951(98)00121-8.

Chester, F.M., and J.S. Chester (2000), Stress and deformation along wavy frictional faults, J. Geophys. Res., 105, 23,421-23,430, doi: 10.1029/2000JB900241.

Chester, F. M., J.S. Chester, D.L. Kirschner, S.E. Schulz, and J.P. Evans, (2004), Structure of large displacement strike-slip faults, in: Rheology and Deformation in the Lithosphere at Continental Margins, Edited by Karner, G. D., B. Taylor, N. W. Driscoll, and D. L. Kohlstedt, Columbia University Press, New York, 2004.

Childs, C., T. Manzocchi, J.J. Walsh, C.G. Bonson, A. Nicol, and M.P.J. Schopfer, (2009), A geometric model of fault zone and fault rock thickness variations, J. Struct. Geo., 31(2), 117-127, doi:10.1016/j.jsg.2008.08.009.

Clauer, N., H. Zwingmann, N. Liewig, and R. Wendling (2012), Comparative 40Ar/39Ar and K–Ar dating of illite-type clay minerals: A tentative explanation for age identities and differences, Earth-Sci. Rev., 115, 76-96, doi: 10.1016/j.earscirev.2012.07.003.

Cowan, D.S., T.T. Cladouhos, and J.K. Morgan (2003), Structural geology and kinematic history of rocks formed along low-angle faults, Death Valley, California, Geol. Soc. Am. Bull., 115, 1230–1248, doi: 10.1130/B25245.1.

Cowie, P. A., and C. H. Scholz (1992), Growth of faults by accumulation of seismic slip, J. Geophys. Res., 97(B7), 11085–11095, doi:10.1029/92JB00586.

Croft, H., K. Anderson, R. E. Brazier, and N. J. Kuhn (2013), Modeling fine-scale soil surface structure using geostatistic, Water Resour. Res., 49, 1858–1870, doi:10.1002/wrcr.20172.

Davidesko, G., A. Sagy, and Y. H. Hatzor (2014), Evolution of slip surface roughness through shear, Geophys. Res. Lett., 41, 1492–1498, doi:10.1002/2013GL058913.

Dieterich, J.H., and B.D. Kilgore (1994), Direct observation of frictional contacts: New insights for sliding memory effects, Pure Appl. Geophys., 143, 283-302, doi: 10.1007/BF00874332.

Dieterich, J.H., and M.F. Linker (1992), Fault stability under conditions of variable normal stress, Geophys. Res. Lett., 19(16), 1691-1694, DOI: 10.1029/92GL01821

Di Toro, G., T. Hirose, S. Nielsen, G. Pennacchioni and T. Shimamoto (2006), Natural and experimental evidence of melt lubrication of faults during earthquakes, Science, 311, 647-649, DOI: 10.1126/science.1121012.

Dokka, R.K. (1984), Fission-track geochronological evidence for late Cretaceous mylonitization and early Paleocene uplift of the northeastern Peninsular Ranges, California, Geophys. Res. Lett., 11, 46-49, doi: 10.1029/GL011i001p00046.

Dorsey, R.J., B.A. Housen, S.U. Janecke, C.M. Fanning, and A.L.F. Spears (2011), Stratigraphic record of basin development within the San Andreas fault system: Late Cenozoic Fish Creek-Vallecito basin, southern California, Geol. Soc. Am. Bull., 123, 771-793, doi: 10.1130/B30168.1.

Dunham, E.M., Belanger, D., Cong, L., and Kozdon, J.E., 2011, Earthquake ruptures with strongly rate-weakening friction and off fault plasticity. Part 2: Nonplanar faults: Bulletin of the Seismological Society of America, v. 101, p. 2308-2322, doi: 10.1785/0120100075.

French, M. E., H. Kitajima, J. S. Chester, F. M. Chester, and T. Hirose (2014), Displacement and dynamic weakening processes in smectite-rich gouge from the Central Deforming Zone of the San Andreas Fault, J. Geophys. Res. Solid Earth, 119, 1777–1802, doi:10.1002/2013JB010757.

Goodwin, L.B., and P.R. Renne (1991), Effects of progressive mylonitization on Ar retention in biotites from the Santa Rosa Mylonite Zone, California, and thermochronologic implications, Contrib. Mineral. Petrol, 108, 283-297, doi: 10.1007/BF00285937.

Ide, S., and M. Takeo (1997), Determination of constitutive relations of fault slip based on seismic wave analysis, J. Geophys. Res., 102(B12), 27379-27391, doi: 10.1029/97JB02675.

Janecke, S.U., R.J. Dorsey, D. Forand, A.N. Steely, S.M. Kirby, A.T. Lutz, B.A. Housen, B. Belgarde, V.E. Langenheim, and T.M. Rittenour (2010), High Geologic Slip Rates since Early Pleistocene Initiation of the San Jacinto and San Felipe Fault Zones in the San Andreas Fault System: Southern California, USA, Geol. Soc. Am. Special Paper 475, 48 p., doi:10.1130/2010.2475.

Johnson, K., E. Nissen, S. Saripalli, J.R. Arrowsmith, P. McGarey, K. Scharer, P. Williams, and K. Blisniuk (2014), Rapid mapping of ultrafine fault zone topography with structure from motion, Geosphere, 10(5), doi: 10.1130/GES01017.1.

Kerry, R., and M. A. Oliver (2007), Determining the effect of asymmetric data on the semi-variogram. I. Underlying asymmetry, Comput. Geosci., 33, 1212–1232, doi: 10.1016/j.cageo.2007.05.009.

Kirkpatrick, J. D. and Brodsky, E. E., 2014, Slickenline orientations as a record of fault rock rheology, Earth and Planet. Sci. Lett., 408, 24-34, doi:10.1016/j.epsl.2014.09.040.

Kitanidis, P.K., 1997, Introduction to Geostatistics, Cambridge University Press, 272 pp.

Lay, T., and H. Kanamori (1981), An asperity model of large earthquake sequences, in Earthquake Prediction, an International Review, Maurice Series, IV, 579-592, AGU, Washington, D.C.

Lay, T., H. Kanamori, and L. Ruff (1982), The asperity model and the nature of large subduction zone earthquakes, Earthquake Predict. Res., 1, 3–71.

Lee, J.J., and R. L. Bruhn (1996), Structural anisotropy of normal fault surfaces, J. Struct. Geol., 18, 1043–1059, doi: 10.1016/0191–8141(96)00022–3.

Lin, A. (2011), Seismic slip recorded by fluidized ultracataclastic veins formed in a coseismic shear zone during the 2008 Mw 7.9 Wenchuan earthquake, Geology, 39(6), 547-550, doi:10.1130/G32065.1.

Linker, M. F., and J. H. Dieterich (1992), Effects of variable normal stress on rock friction: Observations and constitutive equations, J. Geophys. Res., 97(B4), 4923–4940, doi:10.1029/92JB00017.

Lunn, R.J., Z.K. Shipton, and A.M. Bright (2008), How can we improve estimates of bulk fault zone hydraulic properties? in The Internal Structure of Fault Zones: Implications for Mechanical and Fluid Flow Properties, Geol. Soc. London Special Publication, 299, 231-237, doi: 10.1144/SP299.14.

Lyakhovsky, V., A. Sagy, Y. Boneh, Z.E. Reches (2014), Fault wear by damage evolution during steady-state slip, Pure Appl. Geophys, 1 (15). http://dx.doi.org/10.1007/s00024-014-0787-x.

Matti, J.C., D.M. Morton, B.F. Cox, G.P. Landis, V.E. Langenheim, W.R. Premo, R. Kistler, and J.R. Budahn (2006), Fault-bounded late Neogene sedimentary deposits in the Santa Rosa Mountains, southern CA: constraints on the evolution of the San Jacinto Fault, Eos, Trans. AGU, 87(52), Fall Meeting Supplement, Abstract.

Mikumo, T., Y. Yagi, S. K. Singh, and M. A. Santoyo, Coseismic and postseismic stress changes in a subducting plate: Possible stress interactions between large interplate thrust and intraplate normal-faulting earthquakes, J. Geophys. Res., 107(B1), doi:10.1026/2001JB000446, 2002.

Moore, J.C. and D. Saffer (2001), Updip limit of the seismogenic zone beneath the accretionary prism of southwest Japan: An effect of diagenetic to low-grade metamorphism processes and increasing effective stress, Geology, 29(2), 183-186, doi: doi: 10.1130/0091-7613.

Morton, D.M., F.K. Miller, R.W. Kistler, W.R. Premo, C-T.A. Lee, V.E. Langenheim, J.L. Wooden, L.W. Snee, B.L. Clausen and P. Cossette (2014), Framework and petrogenesis of the northern Peninsular Ranges batholith, southern California, Geol. Soc. Am. Mem., 211, 61-143, doi: 10.1130/2014.1211(03).

Nielsen, S., G. Di Toro, and W.A. Griffith (2010), Friction and roughness of a melting rock surface, Geophys. J. Int., 182, 299-310, doi: 10.1111/j.1365-246X.2010.04607.x.

Ohnaka, M. (2013), The Physics of Rock Failure and Earthquakes, Cambridge University Press.

Otsuki, K., T. Uduki, N. Monzawa, and H. Tanaka (2005), Clayey injection veins and pseudotachylyte from two boreholes penetrating the Chelungpu Fault, Taiwan: Their implications for the contrastive seismic slip behaviors during the 1999 Chi‐Chi earthquake, Island Arc, 14(1), 22-36, doi: 10.1111/j.1440-1738.2004.00455.x.

Parsons, T. (2008), Persistent earthquake clusters and gaps from slip on irregular faults, Nature Geosci., 1, 59-63, doi:10.1038/ngeo.2007.36.

Persson, B., 2000. Sliding Friction, Physical Principles and Applications, Springer-Verlag, New York.

Platt, J.D., J. W. Rudnicki, and J. R. Rice (2014), Stability and localization of rapid shear in fluid-saturated fault gouge: 2. Localized zone width and strength evolution, J. Geophys. Res. Solid Earth, 119, 4334–4359, doi:10.1002/2013JB010711.

Power, W. L., T.E. Tullis, S.R. Brown, G.N. Boitnott, G. N., and C.H. Scholz (1987), Roughness of natural fault surfaces, Geophys. Res. Letts., 14, 29-32.

Power, W.L., T.E. Tullis, and J.D. Weeks (1988), Roughness and wear during brittle faulting, J. Geophys. Res., 93(B12), 15268-15,278, doi: 10.1029/JB093iB12p15268.

Reid, H.F. (1910), The Mechanics of the Earthquake, The California Earthquake of April 18, 1906, Report of the State Investigation Commission, Vol.2, Carnegie Institution of Washington, Washington, D.C.

Renard, F., C. Voisin, D. Marsan, and J. Schmittbuhl (2006), High resolution 3D laser scanner measurements of a strike-slip fault quantify its morphological anisotropy at all scales, Geophys. Res. Lett., 33, L04305, doi: 10.1029/2005GL025038.

Rowe, C.R., J.D. Kirkpatrick and E.E. Brodsky (2012), Fault rock injections record paleo-earthquakes, Earth Planet. Sci. Lett., 335-336, 154-166, doi:10.1016/j.epsl.2012.04.015.

Rykl, D. and Pechar, F. (1984), Study relating to temperature stability of the Natural Laumontite Zeolite. Cryst. Res. Technol., 19: 549–555. doi: 10.1002/crat.2170190417.

Sagy, A. and E.E. Brodsky (2009), Geometric and rheological asperities in an exposed fault zone, J. Geophys. Res., 114, B02301, doi: 10.1029/2008JB005701.

Sagy, A., E.E. Brodsky and G.J. Axen (2007), Evolution of fault-surface roughness with slip, Geology, 35, 283-286, doi: 10.1130/G23235A.1.

Scholz, C.H. (1987), Wear and gouge formation in brittle faulting, Geology, 15 (6), 493–495.

Scholz, C.H. (1988), The critical slip distance for seismic faulting, Nature, 336, 761-763, doi: 10.1038/336761a0.

Scholz, C. H. (1998), Earthquakes and friction laws, Nature, 391, 37-42, doi:10.1038/34097.

Scholz, C.H. (2002), The mechanics of earthquakes and faulting, Cambridge, Cambridge University Press, 496 p.

Sharp, R.V. (1967), San Jacinto fault zone of the Peninsular Ranges of southern California, Geol. Soc. Am. Bull., 78, 705-729.

Sharp, R.V. (1979), Some characteristics of the Eastern Peninsular Ranges Mylonite Zone, in Proceedings of the Conference on Analysis of Actual Fault Zones in Bedrock, Open File Report 79, 258–267.

Shi, Z., and S.M. Day (2013), Rupture dynamics and ground motion from 3D rough-fault simulations, J. Geophys. Res., 118, 1122–1141, doi: 10.1002/jgrb.50094.

Sibson, R.H. (1977), Fault rocks and fault mechanisms, J. Geol. Soc. London, 133, 191-213, doi: 10.1144/gsjgs.133.3.0191.

Sibson, R.H. (1986), Brecciation processes in fault zones: inferences from earthquake rupturing, Pure Appl. Geophys., 124(1-2), 159-175, doi: 10.1007/BF00875724.

Sibson, R.H. (2003), Thickness of the seismic slip zone, Bull. Seis. Soc. Am., 93, 1169-1178, doi: 10.1785/0120020061.

Swanson, M.T. (2005), Geometry and kinematics of adhesive wear in brittle strike-slip fault zones, J. Struct. Geo., 27, 871-887, doi: 10.1016/j.jsg.2004.11.009.

Ujiie, K., H. Tanaka, T. Saito, A. Tsutsumi, J.J. Mori, J. Kameda, E.E. Brodsky, F.M. Chester, N. Eguchi, S. Toczko, Expedition 343 and 343T Scientists (2013), Low coseismic shear stress on the Tohoku-Oki megathrust determined from laboratory experiments, Science, 342, 1211-1214, doi: 10.1126/science.1243485.

Verhoeven, G. (2011), Taking computer vision aloft -archaeological three-dimensional reconstructions from aerial photographs with photoscan, Archaeo. Prospect., 18, 67–73, doi: 10.1002/arp.399.

Wang, W., and C. H. Scholz (1994), Wear processes during frictional sliding of rock: A theoretical and experimental study, J. Geophys. Res., 99(B4), 6789–6799, doi:10.1029/93JB02875.

Welch, P.D. (1967), The use of fast Fourier transform for the estimation of power spectra: a method based on time averaging over short, modified periodograms, Audio and Electro. IEEE Trans., 15(2), 70-73, doi: 10.1109/TAU.1967.1161901.

Wenk, H.R., L.R. Johnson, and L. Ratschbacher (2000), Pseudotachylytes in the Eastern Peninsular Ranges of California, Tectonophys., 321, 253–277, doi: 10.1016/S0040-1951(00)00064-0.

White, B.C. (2006), Structural geology of the eastern central Santa Rosa Mountain, Riverside County, California, Masters thesis, 48 pp.

Wilson, J.E., J.S. Chester, and F.M. Chester (2003), Microfracture analysis of fault growth and wear processes, Punchbowl Fault, San Andreas system, California, J. Struct. Geol., 25, 1855-1873.

APPENDIX A: FIELD MAPS

Appendix A: Field Maps

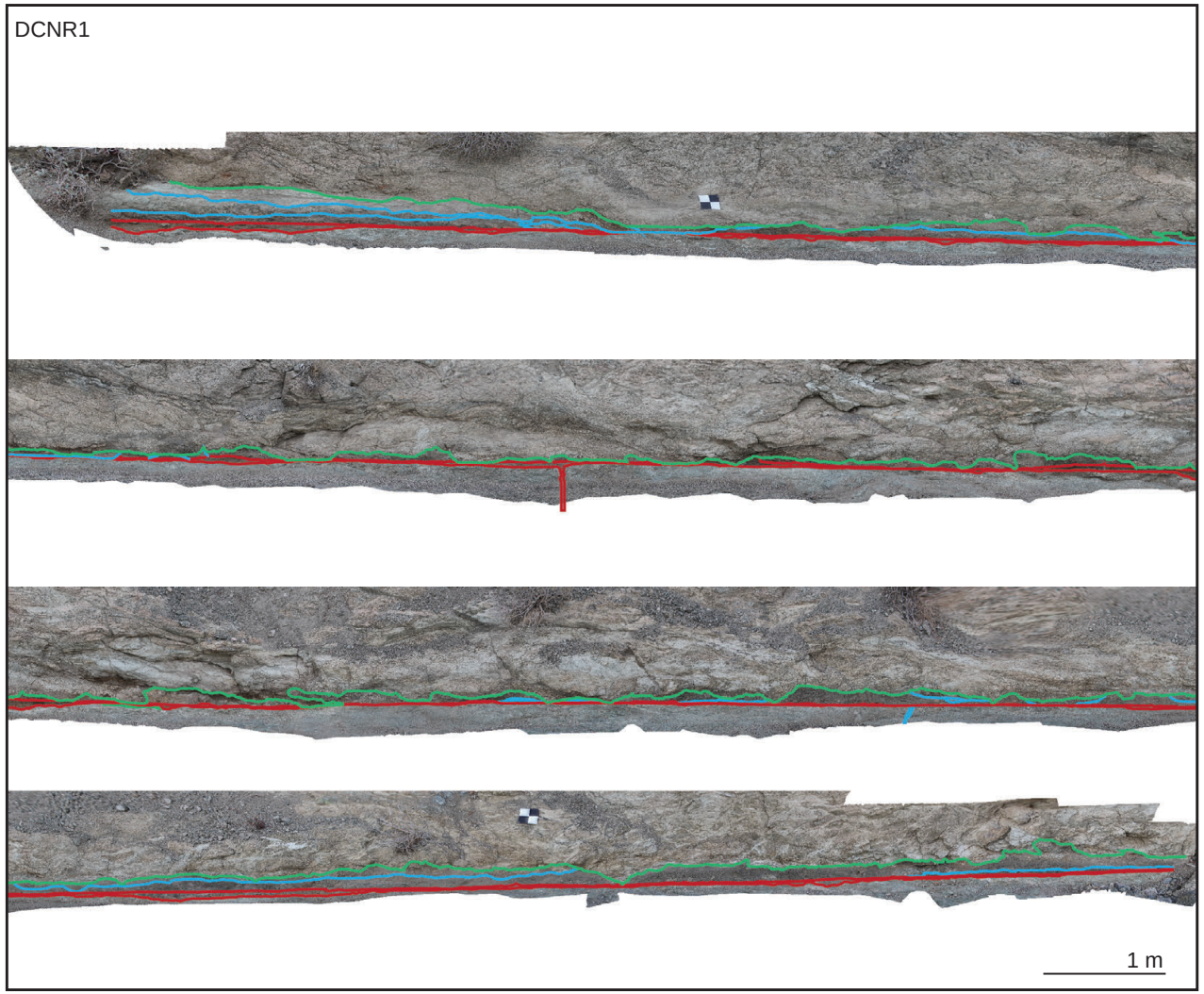

Fig. A1: Field maps of exposure 1. Red is layer d, blue inner fault core layers and green inner-outer fault core contacts. The inner-outer fault core contact is unseen at this location as it is the same as layer d. Top to bottom = downstream to upstream in Coyote Canyon (checked squares are 14 cm across for scale).

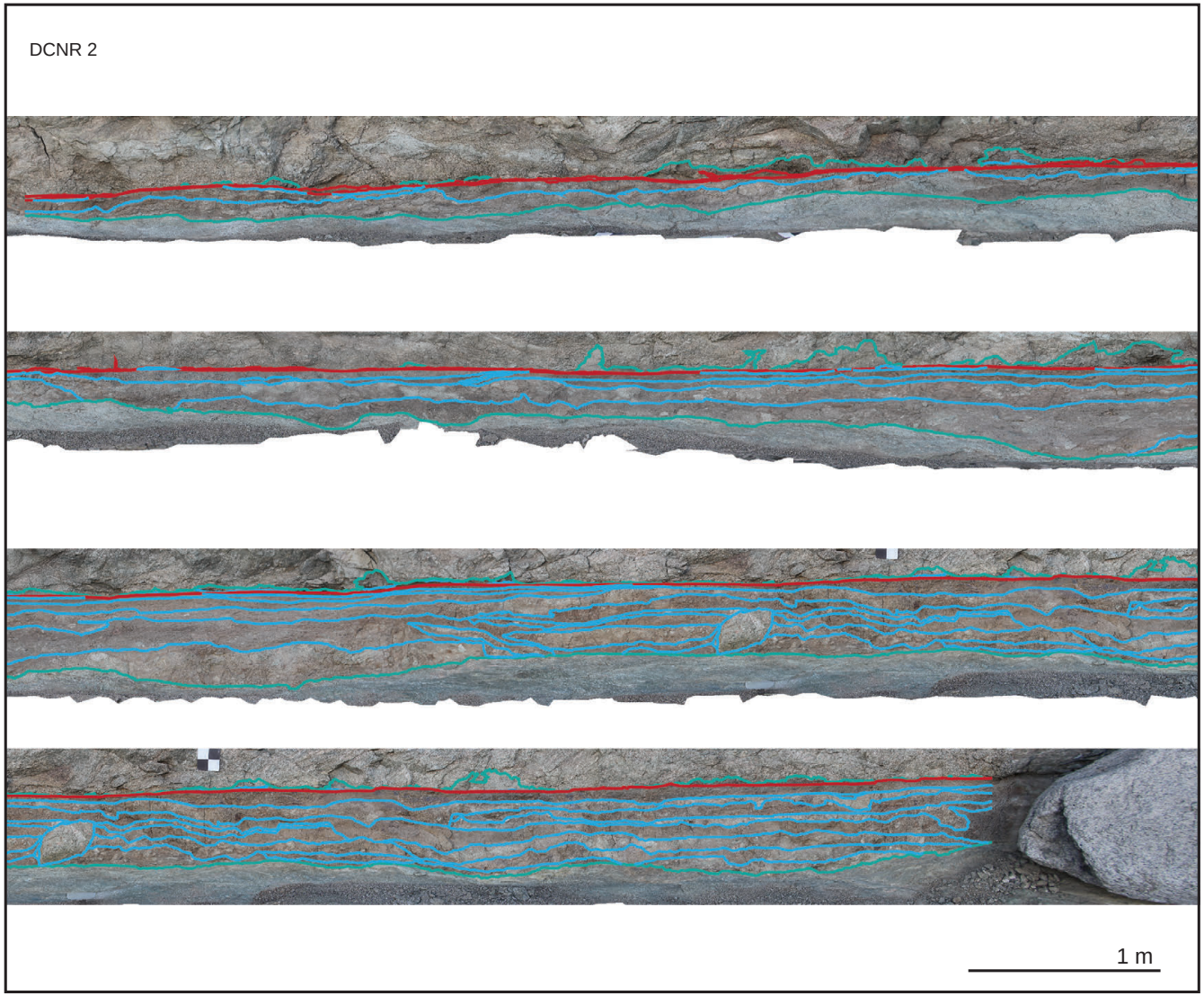

Fig. A2: Field map of exposure 2. Red is layer d, blue inner fault core contacts, and green inner-outer fault core contacts. Top to bottom = downstream to upstream.

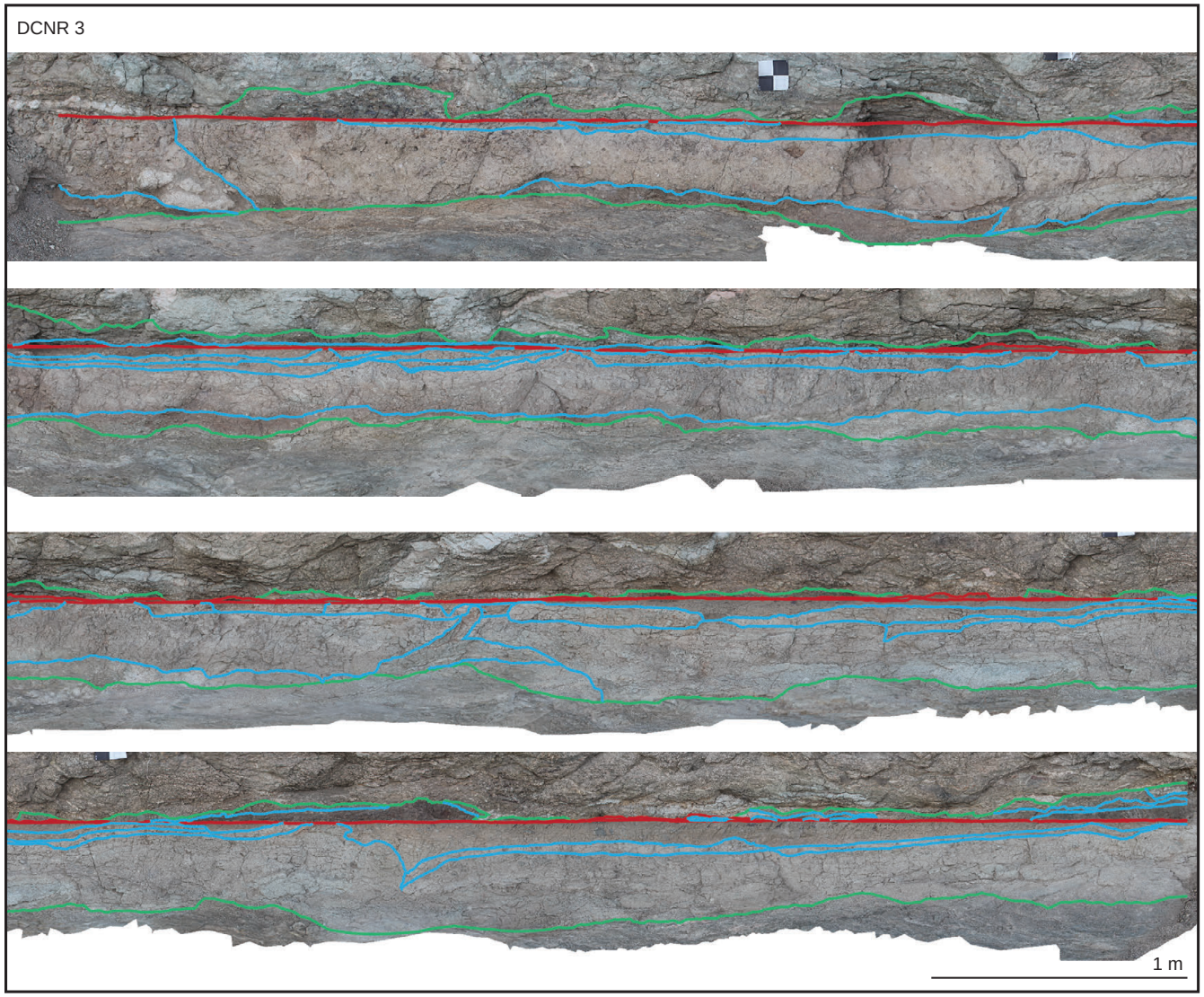

Fig. A3: Field map of exposure 3. Red is layer d, blue inner fault core, and green inner-outer fault core contacts. Top to bottom = downstream to upstream.

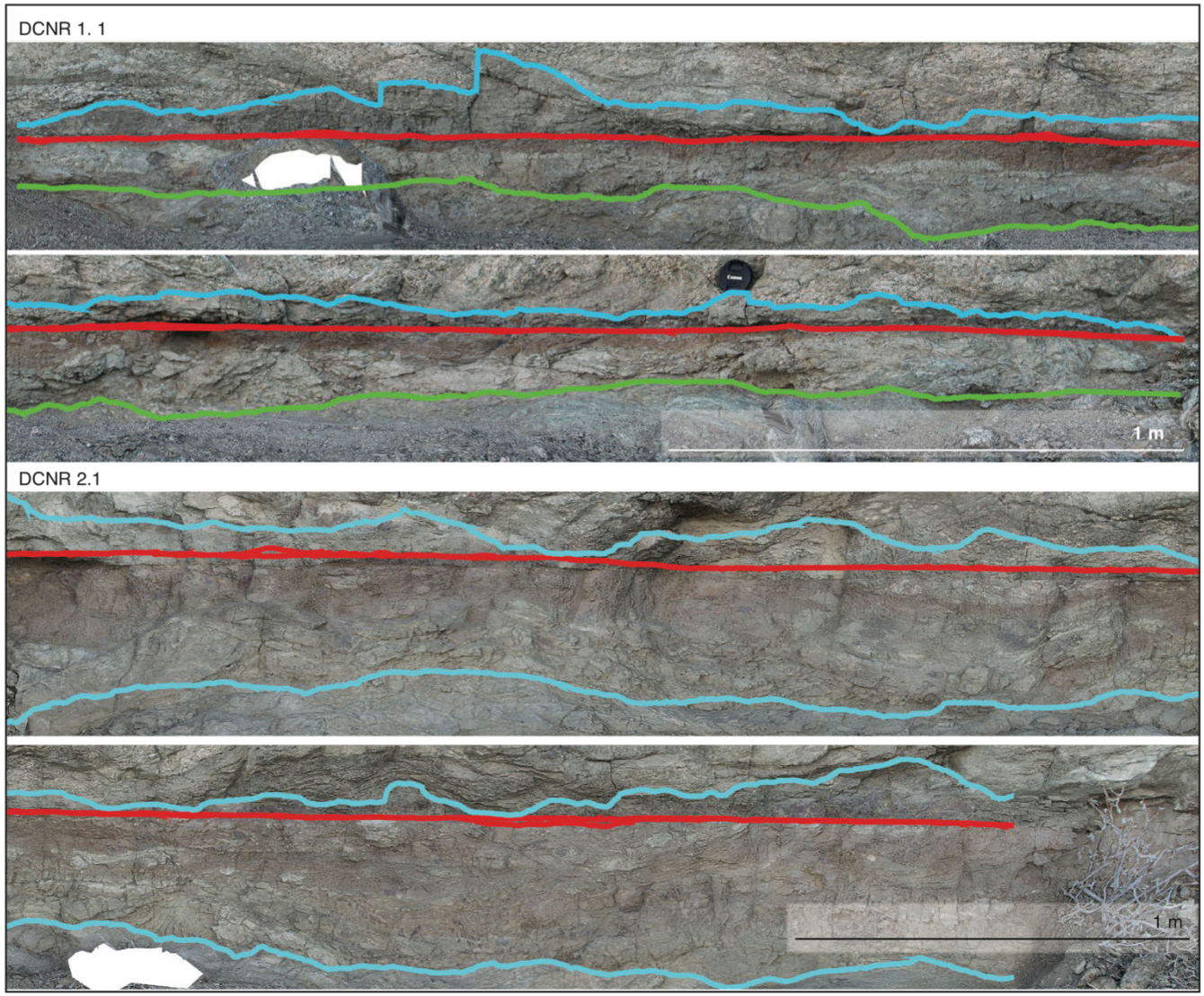

Fig A4: Field maps of exposure 1.1 (between exposures 1 and 2) and 2.1 (between exposures 2 and 3). For 1.1, red is layer d, blue is the upper-outer fault core contact, and green is the lower-outer fault core contact. For 2.1, red is layer d, and blue is inner-outer fault core contacts. The internal structure of the fault core was mapped in the field, but not transferred to high-resolution maps. White holes are cropped-out features in the model that obstructed the view of the fault core.

APPENDIX B: XRD RESULTS

Appendix B: XRD results

Table B1. XRD results from multiple samples of the upper-outer fault core (HW), the inner fault core (IFC), layer d, and the lower-outer fault core (FW). Synthesized versions of these results were presented in the paper and Figure 2a.

Loc.	HW	HW	layer d	IFC-	IFC	FW	FW	FW	FW	FW	FW	IFC
Sample	X-1	X-3	X-4	X-5	X-6	X-7	X-8	X-9*	X-10	X-13	X-14	X-15*
Quartz	25%	20%	15%	40%	20%	25 %	30%	35%	15%	20%	40%	50%
Anorthite, sodian	10%	15%		present		35 %	40%	45%	50%			20%
Labradorite			30%									
Albite	35%	25%		30%	50%					60%	30%	10%
Heulandite-Ca												present
Laumontite	10%		10%	15%	15%						25%	present
Chamosite		15%	5%	10%		5%	5%	present		5%	5%	
Illite							15%	15%	25%			present
Chlorite	15%			5%					present			present
Epidote		10%				10 %	5%	present		10%		present
Hastingsite												
Actinolite	10%				present							
Brucite		5%										
Jarosite		5%										
Titanomagnetite		present										

Cronstedtite		present										
Clinochlore					20%				5%			
Rutile										5%		
Calcite								present	5%			
Amorphous	35 %											

* indicates some peaks present in sample spectrum were not satisfactorily matched to reference library - possibility of additional phases present.
"present" means the peaks for this mineral are definitely in the sample spectrum, abundance < ~ 5%
Mineral modal % are approximate (uncertainty is not quantified but analysis results are reproducable to about +/- 5%.

APPENDIX C: PHOTOSCAN REPRODUCIBILITY TEST

Appendix C: Photoscan reproducibility test

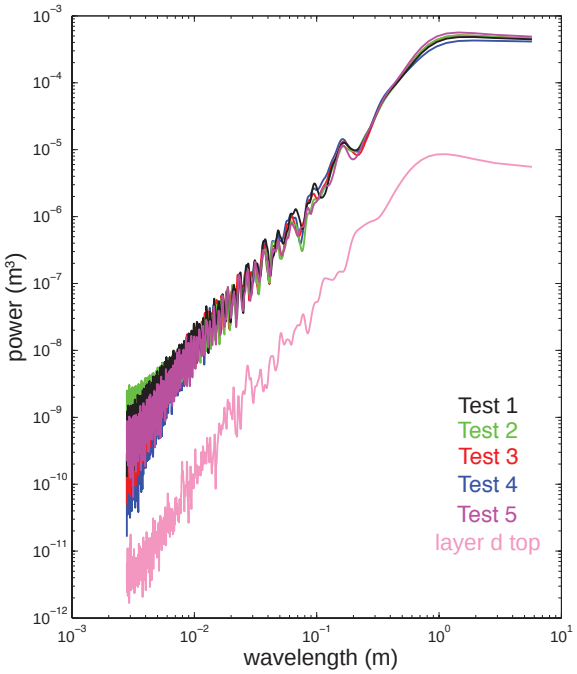

Figure C1: Power spectral density of the precision test traces of the hanging wall contact in black, green, red, blue and purple. The pink line is the trace of the top of layer d at the same exposure as a comparison.

Photoscan Pro generates a slightly different model from the same input photos every time it is used. To test if this affected the significance of our results, we used one set of photos from a small exposure not analyzed for this work and generated 5 models using the same parameters. Each model was rotated in the direction of the slip vector, exported and inner fault core top trace was mapped. Figure D1 shows the power spectral density results of the precision test. The five test traces overlap at all wavelengths. There is no overlap between the top of layer d and the test traces (shown for reference). The slopes of the test traces range from 2.15-2.30, consistent with slopes of less than 3 presented in the paper. At wavelengths greater than 10^{-2}, or a majority of the wavelengths represented on this plot, the traces have the same shape and follow each other closely. At wavelengths below 10^{-2}, variability between the test traces is greater, but is still small compared to the difference between the test traces and the trace of the top of layer d. We interpret the noise at short wavelengths in the test traces as a result of a combination of the resolution of the texture in the generated models and operator variability in mapping small-scale features. As discussed in the main text, our roughness measurements using Photoscan Pro are

within the range of observed values from terrestrial laser scanner surveys. We conclude the precision of the measurements is such that the uncertainty for individual traces is less than the difference between individual traces, and therefore the precision is high enough that our interpretation of our results is significant.

APPENDIX D: HISTOGRAMS AND STATIONARITY TEST

Appendix D: Histograms and Stationarity Test

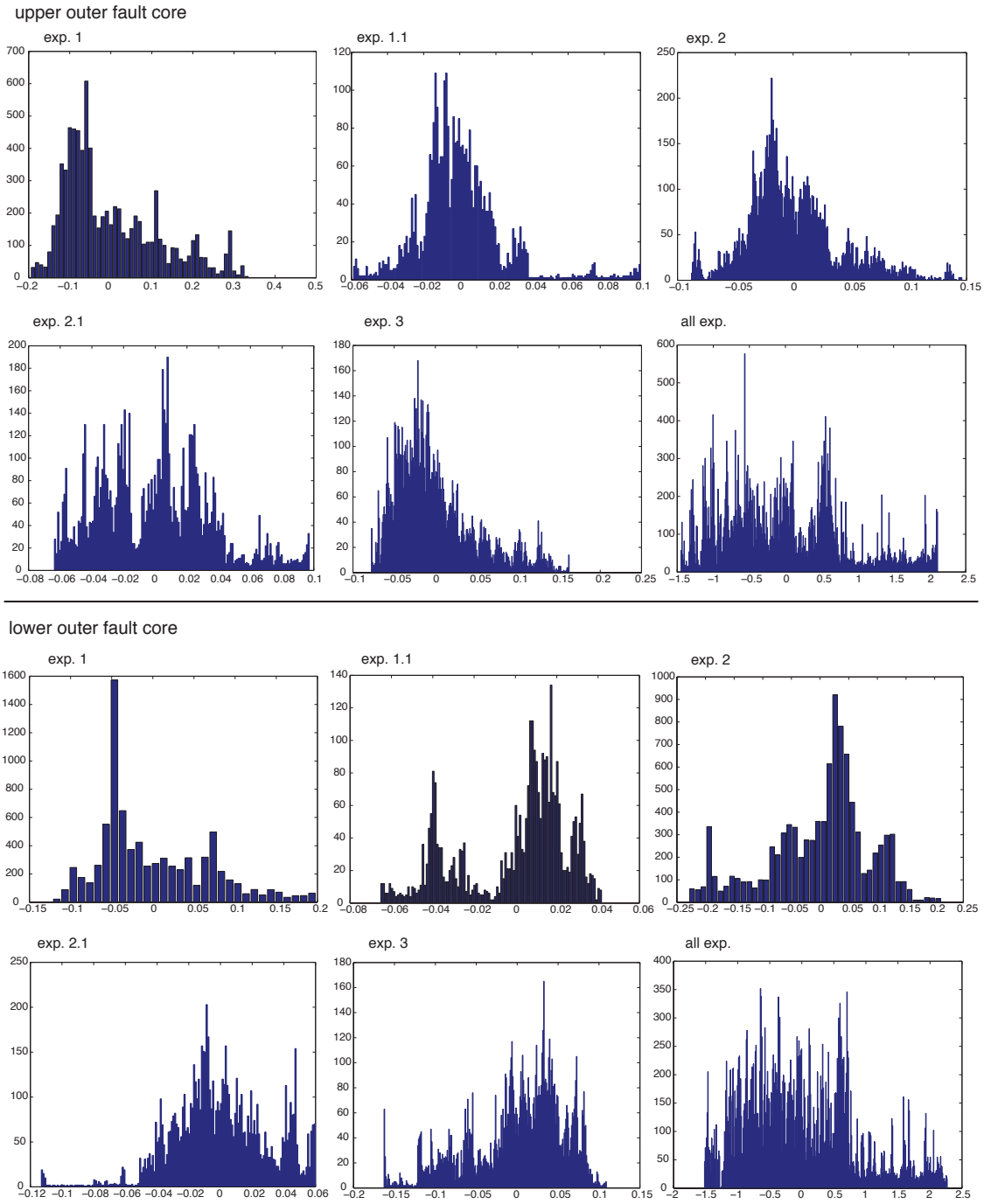

Fig. D1: Histograms of the detrended data used for PSD and variogram analysis of the inner-outer fault core contacts. Histograms plotted for exp. 1, 1.1, 2, 2.1, 3 and all exposures.

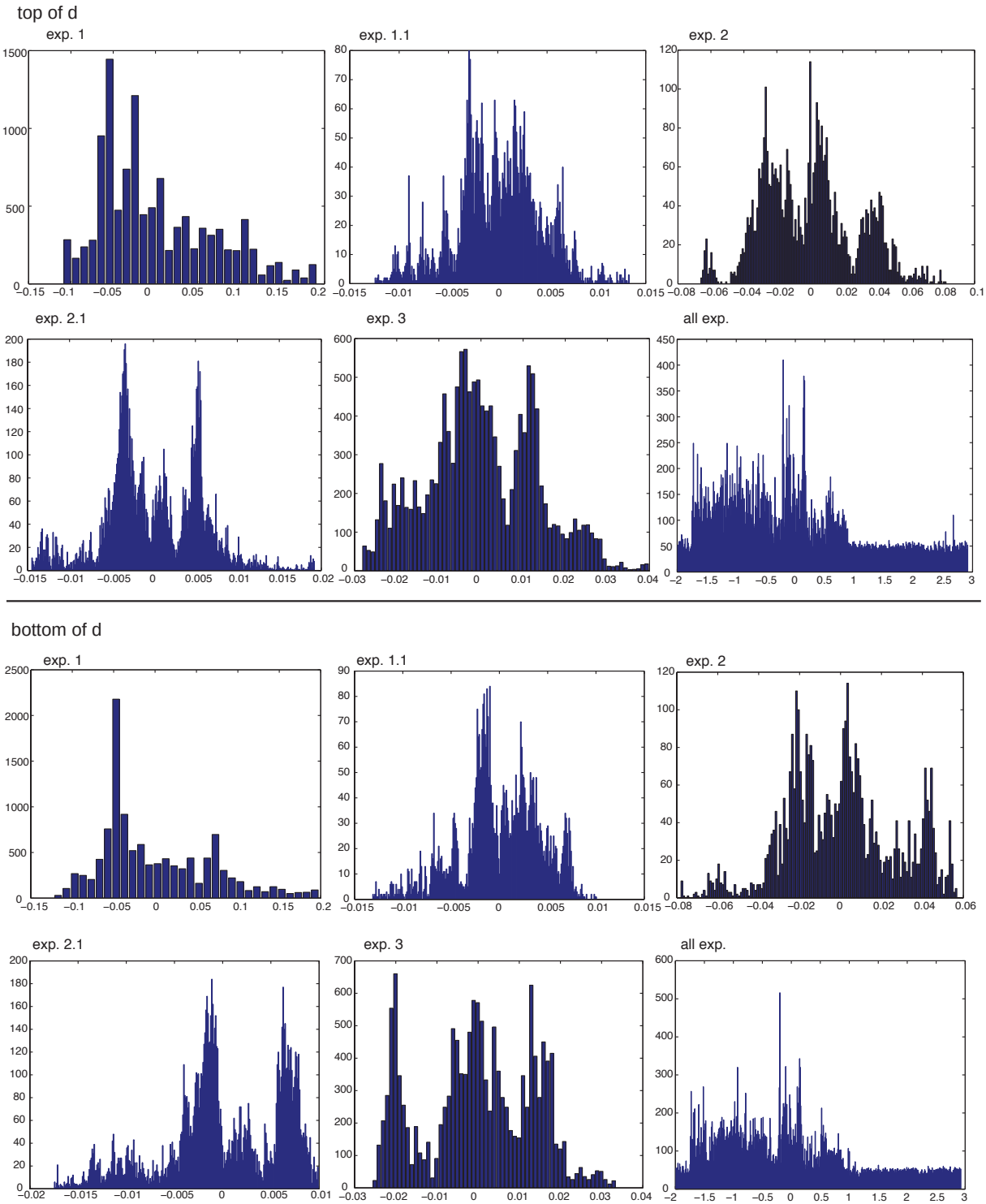

Fig. D2: Histograms of the top and bottom detrended contacts of layer d. Histograms were plotted of exp. 1, 1.1, 2, 2.1 and 3 as well as all exposures.

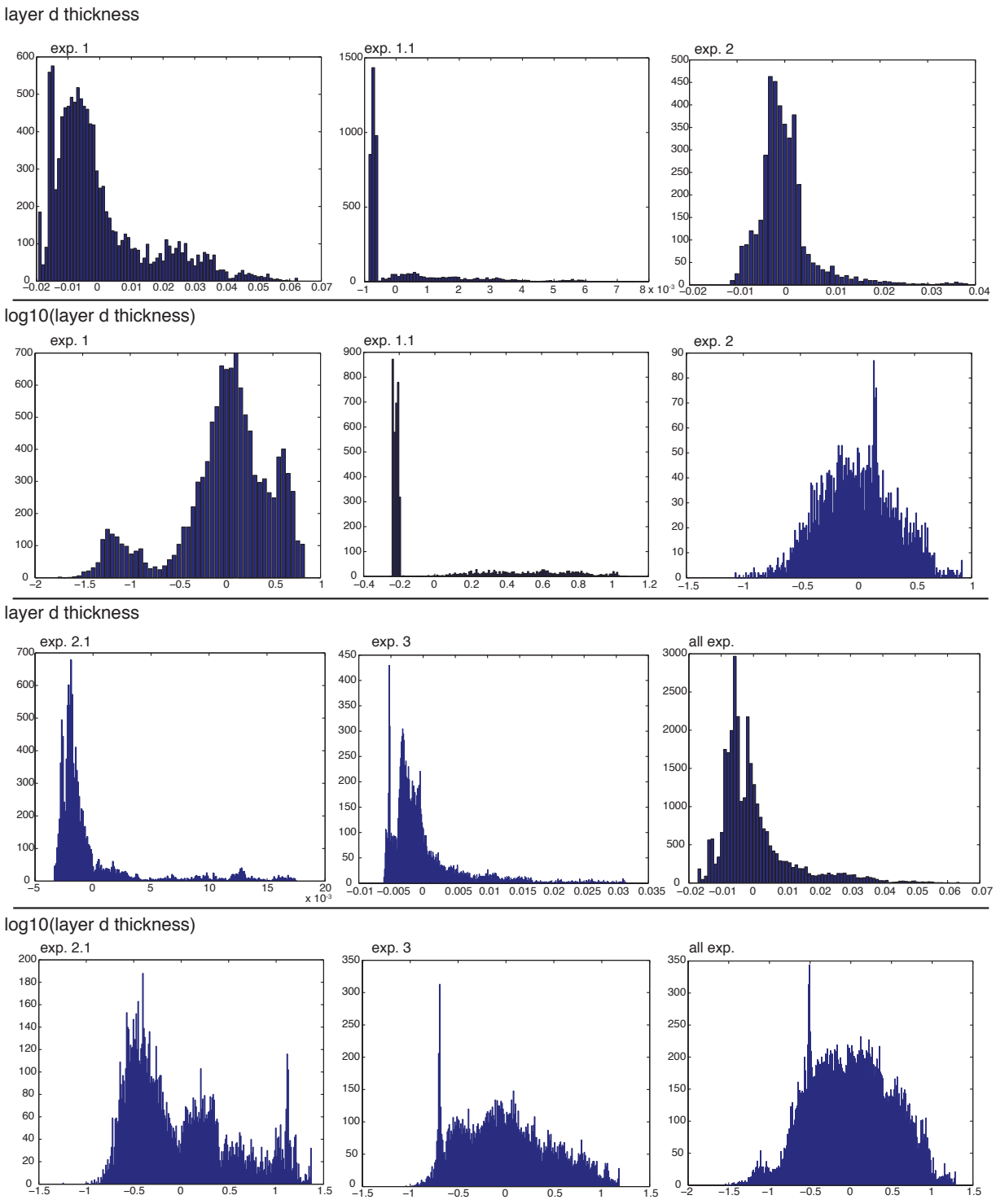

Fig. D3: Histograms of layer d thickness. The histogram of detrended data is presented in one row and the row below shows the histogram of log10-transformed data. Exp. 1, 1.1, 2, 2.1 and 3 as well as all data are plotted.

Stationarity

Data is considered weakly stationary (WSS) if the datasets tested have the same mean, variance, and an autocovariance that does not depend on space. Because the data is detrended before we use it for analysis, the mean of each trace is approximately zero. The variance of each trace at all exposures and layer d thickness at all exposures was compared using an f-test for equal variances. The variances are tested against the null hypothesis that they come from the same distribution with the same variance (h=0). The other option is they come from different distributions with different variances (h=1). The p-value indicates the probability of observing an extreme value and when low or close to zero, indicates the null hypothesis is invalid. Generally, all exposures do not have the same variance. Only one pair of exposures for the upper-outer fault core represent the same population: exposures 2 and 2.1, which are next to each other.

Table D1: The results of an f-test to determine whether the variances of a data set came from the same distribution. The first value in the brackets is h. When h is 1, the variances are from different distributions. When h is 0, the variances are from the same distribution. The second value is the p-value, indicating the probability of the variances originating from the same distribution.

[h,p]	upper outer fault core	lower outer fault core	top of d	bottom of d
1 vs. 1.1	[1, 0]	[1, 0]	[1, 0]	[1, 0]
1 vs. 2	[1, 0]	[1,0.000002]	[1, 0]	[1, 0]
1 vs. 2.1	[1, 0]	[1, 0]	[1, 0]	[1, 0]
1 vs. 3	[1, 0]	[1,0.000003]	[1, 0]	[1, 0]
1.1 vs. 2	[1,0.000001]	[1, 0]	[1, 0]	[1, 0]
1.1 vs. 2.1	[1,0.000001]	[1, 0.0000005]	[1, 0.000007]	[1,0.0000001]
1.1 vs. 3	[1, 0]	[1, 0]	[1, 0]	[1, 0]
2 vs. 2.1	[0,1]	[1, 0]	[1, 0]	[1, 0]
2 vs. 3	[1,0.000001]	[1, 0]	[1, 0]	[1, 0]
2.1 vs. 3	[1,0.000001]	[1, 0]	[1, 0]	[1, 0]